Charles University in Prague
Faculty of Mathematics and Physics

MASTER THESIS

Markéta Jansová

Analysis of Diffractive Open Charm Photoproduction with a Leading Proton at HERA

Institute of Particle and Nuclear Physics

Supervisor of the master thesis: RNDr. Karel Černý, Ph.D.
Study programme: Physics
Specialization: Nuclear and Particle Physics

Prague 2015

I would like to thank to my supervisor RNDr. Karel Černý, Ph.D. and consultants Mgr. Radek Žlebčík and RNDr. Alice Valkárová, DrSc. for their valuable help and advice. Also my thanks go to my family and friends who have supported me during the studies.

I declare that I carried out this master thesis independently, and only with the cited sources, literature and other professional sources.

I understand that my work relates to the rights and obligations under the Act No. 121/2000 Coll., the Copyright Act, as amended, in particular the fact that the Charles University in Prague has the right to conclude a license agreement on the use of this work as a school work pursuant to Section 60 paragraph 1 of the Copyright Act.

In .... date ....

Název práce: Analýza volné produkce charm kvarku v difrakční fotoprodukci s elastickým protonem v koncovém stavu na HERA

Autor: Markéta Jansová

Katedra: Ústav částicové a jaderné fyziky

Vedoucí diplomové práce: RNDr. Karel Černý, Ph.D.

Abstrakt: Difrakční volná produkce charm kvarku je studována s použitím dat získaných s pomocí detektoru H1 v letech 2006-2007. V tomto období bylo možné měřit rozptýlený proton s využitím dopředného detektoru protonů na H1 zvaného VFPS. Produkce charm kvarku je zkoumána v rozpadech D^* mezonu. Účinný průřez procesu $e^+p \to e^+D^*X'p$ ve fotoprodukčním režimu definovaným hodnotou virtuality fotonu $Q^2 < 2\,\mathrm{GeV}$ byl změřen a srovnán s MC Rapgap předpovědí na hadronové úrovni, která je založená na difrakčních partonových distribučních funkcích získaných z inkluzivního hluboce nepružného ep rozptylu.

Měření rozptýleného protonu představuje jedinečnou možnost zkoumat odezvu dopředných detektorů pro elastické případy. S pomocí těchto interakcí je prověřena platnost výběru difrakčních případů metodou LRG.

Klíčová slova: difrakce, fotoprodukce, charm kvark, D^* mezon, VFPS

Title: Analysis of Diffractive Open Charm Photoproduction with a Leading Proton at HERA

Author: Markéta Jansová

Department: Institute of Particle and Nuclear Physics

Supervisor: RNDr. Karel Černý, Ph.D.

Abstract: The diffractive open charm production is studied using data from 2006-2007, when the leading proton measurement by H1 Very Forward Proton Spectrometer was provided. The charm production is tagged by the decay products of D^* meson. The cross section of $e^+p \to e^+D^*X'p$ in photoproduction regime defined by the value of virtuality $Q^2 < 2\,\mathrm{GeV}$ is determined and corrected for the detector effects. The diffractive D^* meson photoproduction cross section is compared with the hadron level MC Rapgap prediction based on diffractive parton distribution functions extracted from inclusive ep DIS measurements.

Measurement of leading proton provides a unique opportunity to investigate the response of forward detectors for the diffractive events. Using such events, the performance of the large rapidity gap selection is examined.

Keywords: diffraction, photoproduction, charm quark, D^* meson, VFPS

Contents

Introduction

Deep-inelastic scattering processes (DIS) played a crucial role in an investigation of the proton structure. Experimental results on DIS in conjuncture with the theoretical explanations have led to the picture of proton as a composite object consisting of quarks and gluons – building blocks of the theory of strong interactions, Quantum Chromodynamics (QCD).

In high energy physics there exist so-called diffractive processes in which no quantum numbers between initial and final state are exchanged. It is known that a significant fraction of hadron-hadron collisions is represented by the diffractive processes. The vast majority of these processes cannot be described by the perturbative QCD (pQCD). Nevertheless, there are diffractive processes where a hard scale is involved, which allows us to study the nature of diffraction in terms of pQCD.

The experimental results have shown that gluons in the proton play the major role in diffractive processes. One of the processes sensitive to the gluon content of proton is the production of heavy quarks in DIS.

Part I

D^* analysis

1. Theoretical overview

1.1 Theory of strong interactions

Quantum Chromodynamics (QCD) is a theory of strong interactions based on $SU(3)$ color symmetry [1]. Color is the property which distinguishes quarks from leptons since leptons have no color and quarks do. It can be said that color plays a role in QCD like electric charge in Quantum Electrodynamics (QED). Consequently, the theory of strong interactions was built on non-Abelian local color gauge symmetry.

In general the higher orders of perturbative expansion give infinite contributions to the total cross section. Therefore, these unphysical infinities have to be eliminated by renormalization process, which introduces theoretical bare quantities. Consequently, the coupling constants of field theories depend on distance, for example after applying renormalization procedure the electric charge is infinite while being near and with distance decreases - is screened. In contrary to electroweak interaction, the coupling constant of strong interaction grows at large and decreases at small distances, thus is antiscreened [2]. Such theory is called asymptotically free.

1.2 Deep-inelastic scattering

A valuable tool for studying proton structure is scattering of leptons on protons in a so-called deep inelastic (DIS) regime. Lepton interacts via electroweak gauge boson at large four-momentum transfer squared Q^2 which probes structure of the proton. Wavelength λ of intermediate boson is related to Q^2 as $\lambda \sim 1/Q$, thus for small Q^2 the wavelength is large and proton seems to be structureless, but with increasing Q^2 the resolution becomes better and structure of proton starts to appear.

Deep-inelastic scattering is an interaction of type

$$l(k) + p(P) \to l'(k') + X, \tag{1.1}$$

illustrated in Fig. 1.1. Where $l(k)$ and $l'(k')$ represent the incoming and outgoing leptons with their four-momenta, respectively. Further $p(P)$ is the incoming proton with four-momentum P and the hadronic final state is generically labeled as X. Two types of the above process are distinguished – neutral and charged current. Neutral current processes are mediated by exchange either of γ or Z^0 and, in this case, the lepton remains unchanged. In contrary in charged current processes incoming and outgoing leptons' charges differ by ±1. These processes are mediated by an exchange of $W^{\pm}$.

For DIS, the following kinematic variables can be introduced

$$s = (k + P)^2, \tag{1.2}$$

$$q = k - k',\ Q^2 = -q^2, \tag{1.3}$$

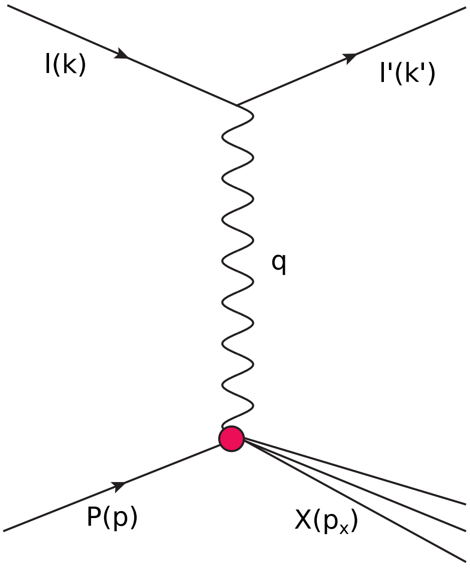

Figure 1.1: The Feynman diagram of lepton-proton inelastic scattering.

$$y = \frac{Pq}{Pk}, \tag{1.4}$$

$$x = \frac{Q^2}{2Pq}, \tag{1.5}$$

$$W = \sqrt{(q+P)^2}, \tag{1.6}$$

where s is the center of mass energy squared, Q^2 the negative lepton four-momentum transfer squared (photon virtuality). The value of inelasticity y corresponds to the relative energy loss of the lepton in the proton rest frame. Variable x can be interpreted within a parton model as a fraction of the proton momentum carried by the struck proton constituent in the proton infinite momentum frame. And finally W represents the invariant energy of the hadronic final state X.

1.2.1 The parton model

In order to describe lepton-proton scattering, the square of invariant matrix element can be written as

$$\overline{|\mathcal{M}|^2} = \frac{e^4}{q^4} L^{\mu\nu} W_{\mu\nu}, \tag{1.7}$$

where $L^{\mu\nu}$ is leptonic tensor given by QED and $W_{\mu\nu}$ hadronic tensor where holders of indices are four-momenta P and q and metric tensor [3]. Under certain theoretical physically well defined assumptions the general formula for differential cross section in x and Q^2 of inelastic scattering can be expressed [3]

$$\frac{\mathrm{d}\sigma}{\mathrm{d}x\mathrm{d}Q^2} = \frac{4\pi\alpha_{em}^2}{xQ^4}\left[\left(1 - y - \frac{M^2xy}{2kP}\right)F_2(x,Q^2) + \frac{1}{2}xy^2 2F_1(x,Q^2)\right], \tag{1.8}$$

where M is the proton mass, α_{em} fine structure constant, $F_1(x, Q^2)$ and $F_2(x, Q^2)$ so called proton structure functions.

The early measurements of DIS at SLAC have shown the lack of dependence of the proton structure functions on the Q^2 for fixed x values [4], so called structure function (or Bjorken) scaling. This observation subsequently led to the formulation of the parton model. In the parton model framework, the fast moving proton can be viewed as being composed of free partons each carrying momentum fraction of the incoming proton [1]. Therefore in the parton model the DIS cross section can be described as an incoherent sum of scattering cross sections on individual charged fermions [3].

In consequence, the dependence on Q^2 can be omitted from proton structure function. The form of $F_2(x)$ is given by

$$F_2(x) = x \sum_i e_i^2 f_i(x), \tag{1.9}$$

where $f_i(x)$ is probability density function of finding parton of type i with momentum fraction x, so called parton distribution function. Parton model can also predict $F_1(x)$ as a function of $F_2(x)$. In case of spin 1/2 parton the relation called Callan-Gross is

$$F_1(x) = \frac{1}{2x} F_2(x). \tag{1.10}$$

In parton model the momentum sum rule

$$\sum_i \int_0^1 \mathrm{d}x \; x f_i(x) = 1 \tag{1.11}$$

corresponds to the fact that total proton momentum must be carried by proton constituents. From the measurements, it was found out that charged partons contribute only by about one half to the total proton momentum [5]. This means that approximately half of proton momentum must be also carried by neutral partons which were eventually identified as gluons.

Finally, the partons were identified to be the basic fields of Quantum Chromodynamics carrying a new quantum number named color, which in turn did fit into the additive quark model of hadrons [6], in which the newly introduced quantum number was needed in order to preserve the symmetry properties of hadrons' wavefunctions. In QCD framework, quarks can be in one of the three color states. Further, there are 8 color states of the gluon. QCD is so called asymptotically free theory, this means, that on short distances quarks and gluons are quasi-free, but with increasing distance the strength of interaction grows and thus the colored quarks and gluons are confined inside hadrons. Due to this property of QCD only colorless hadrons are observed.

1.2.2 Parton distribution functions

The determination of parton distribution functions (PDFs) introduced in (1.9) was the main goal of the physics program at HERA collider, DESY. The parton distribution functions were primarily extracted from inclusive DIS measurements [7]. Within the QCD, the PDFs are expected not to be constant with

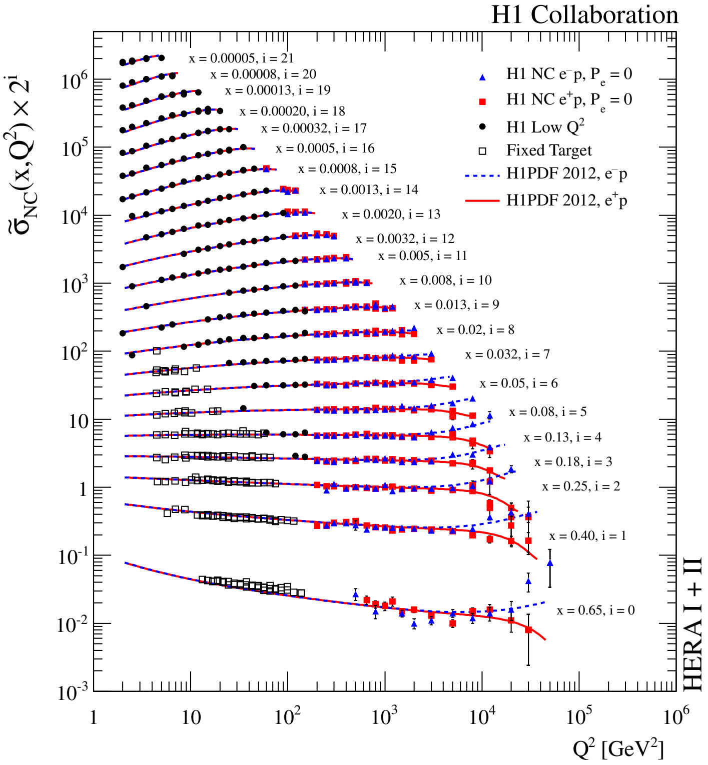

Figure 1.2: Neutral current reduced cross sections $\tilde{\sigma}_{NC} \simeq F_2$ for $e^{\pm}p$ scattering for both HERA-I, HERA-II periods [7].

increasing Q^2 in contrast with parton model because partons are interacting objects. This violation of Bjorken scaling is depicted in Fig. 1.2. Further evolution of quark and gluon distribution functions is described by DGLAP equations

$$\frac{\mathrm{d}q_j(x,\mu_f^2)}{\mathrm{d}\ln\mu_f^2} = \frac{\alpha_s(\mu_f^2)}{2\pi}(P_{qq}^0 \otimes q_j + P_{qg}^0 \otimes g), \tag{1.12}$$

$$\frac{\mathrm{d}g(x,\mu_f^2)}{\mathrm{d}\ln\mu_f^2} = \frac{\alpha_s(\mu_f^2)}{2\pi}(\sum_j P_{gq}^0 \otimes q_j + P_{gg}^0 \otimes g), \tag{1.13}$$

where j runs over quark and antiquark flavors, μ_f^2 is scale which is in DIS usually identified with Q^2 and P_{gg}, P_{qg}, P_{gq} and P_{qq} are the splitting functions [3]. In Fig. 1.3 the parton distribution functions for scale $\mu_f^2 = 10\,\mathrm{GeV}^2$ are shown.

1.3 Diffraction

It is known that a significant fraction of hadron-hadron collisions is represented by the diffractive processes. The vast majority of these processes cannot be described by the perturbative QCD (pQCD), because the scattering cross section is represented by interactions at low momentum transfers. Nevertheless, analytic properties of the scattering amplitude can be studied as a function of an angular momentum in the complex plane, so-called Regge theory [8]. Partial wave analysis

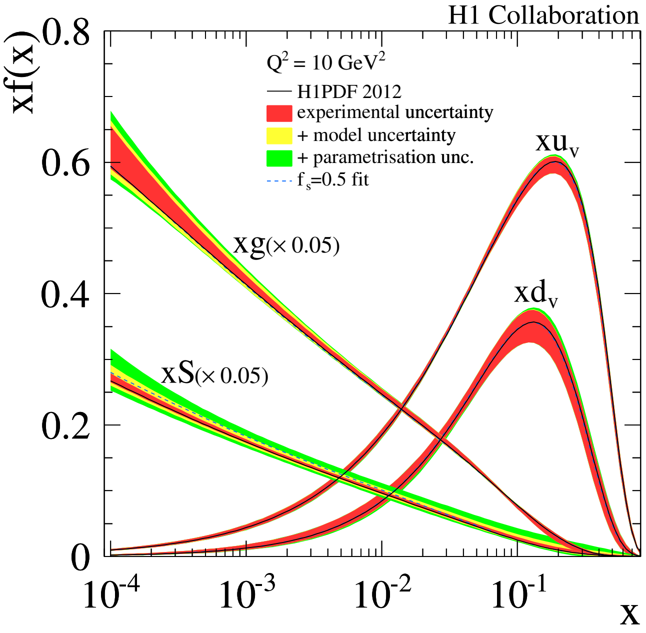

Figure 1.3: Parton distribution functions at $\mu_f^2 \equiv Q^2 = 10\,\mathrm{GeV}^2$ [7].

led to an introduction of so called Regge trajectories (one of them is depicted in Fig. 1.4), which represent a generalization of a single particle t-channel exchange model. The Regge trajectories can be assigned to series of known mesons or baryons. It was found by Donnachie and Landshoff [9] that in order to describe the energy dependence of the total hadron-hadron cross section an additional trajectory with quantum numbers of the vacuum needed to be introduced, so called pomeron $I\!P$ [9, 10, 11].

Diffractive processes in particle collisions at high energies are explained by pomeron exchange, which has also consequences to kinematics of final states. General definitions of diffraction can be formulated as follows. A reaction in which no quantum numbers are exchanged between the colliding particles is, at high energies, a diffractive reaction [12]. Or it can be said the diffractive processes are those, in which a large non-exponentially suppressed gap in rapidities (defined in Sec. 5.1) is observed.

So far, it was assumed that diffraction is a soft phenomenon and perturbative QCD is useless in this case. However, in 1984 Ingelman and Schlein predicted [13] that the diffractive processes may involve hard scale and this hypothesis was actually experimentally confirmed in 1988, when jets were observed in $pp(p\bar{p})$ diffractive interactions at UA8 [14].

Processes described above are called diffractive due to a similarity with optics via the behavior of their forward scattering amplitudes.

1.3.1 Diffractive DIS

The diffractive DIS processes

$$e(k) + p(P) \rightarrow e(k') + p(P') + X, \tag{1.14}$$

or

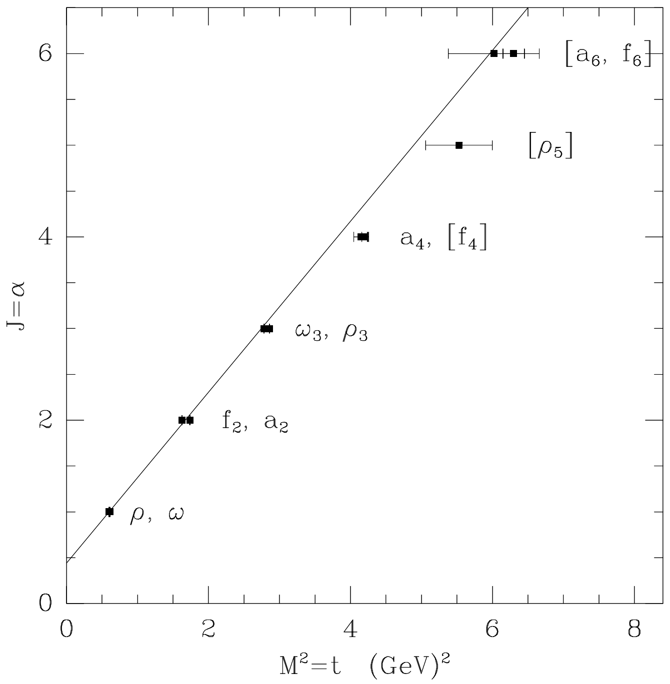

Figure 1.4: The leading meson Regge trajectory which describes dependence of the spin J on the mass squared of the resonances [9].

$$e(k) + p(P) \to e(k') + Y(P') + X, \tag{1.15}$$

where the proton remains intact (1.14) or dissociates into a relatively small mass hadronic state Y (compared with W) (1.15) which is separated from system X by a large rapidity gap are called diffractive deep-inelastic scattering.

In Fig. 1.5 a Feynman diagram corresponding to (1.14) is shown. In addition to standard DIS the diffractive one introduces further kinematic variables

$$x_{IP} = \frac{q(P - P')}{qP}, \tag{1.16}$$

$$t = (P - P')^2, \tag{1.17}$$

where x_{IP} is fractional proton momentum loss and t is four-momentum transfer squared at the proton vertex. The basis of such process

$$\gamma^* p \to Xp, \tag{1.18}$$

is called single dissociation of virtual photon and is shown in Fig. 1.6.

In H1, the observation that diffractive contribution needs to be taken into account for DIS was made in 1994 [15]. In Fig. 1.7 a distribution of detector quantity sensitive to a rapidity gap spanning between the most forward hadronic final state (HFS) candidate and undetected leading proton is shown. As can be seen, the non-diffractive model (exponentially suppressed) is not sufficient to describe data with LRG.

The differential cross section of $\gamma^* p$ DDIS in x, Q^2, x_{IP} and t can be written as

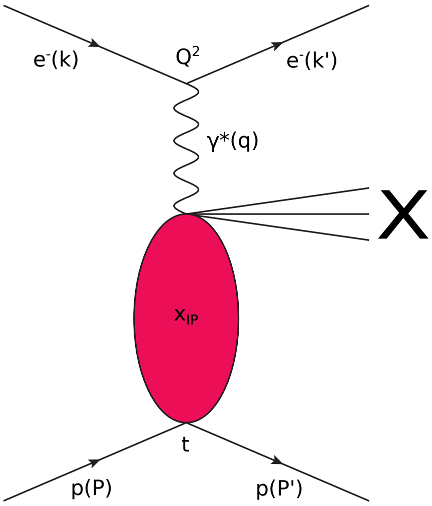

Figure 1.5: Feynman diagram of the diffractive deep-inelastic $e^{-}p$ scattering mediated by pomeron exchange.

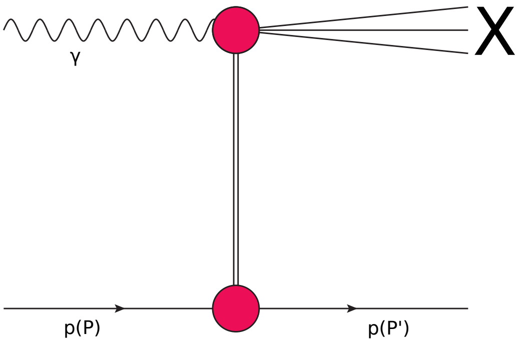

Figure 1.6: The Feynman diagram of the diffractive process $\gamma p \to Xp$, where p and X are separated by the LRG. In this process, γ dissociates into the system X while p remains intact and therefore the process is called single dissociation.

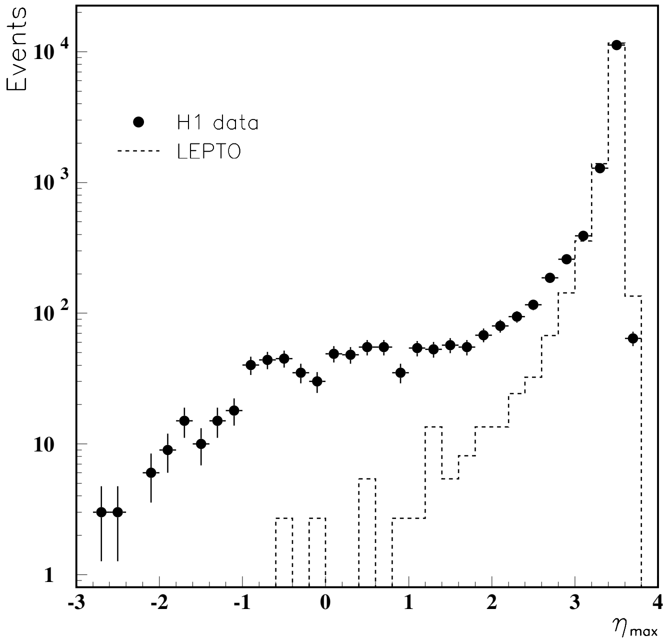

Figure 1.7: Distribution of the pseudorapidity η_{max} of the most forward cluster in H1 detector in DIS as measured by H1 collaboration. The theoretical non-diffractive MC prediction is shown in dashed line [15].

$$\frac{\mathrm{d}\sigma^D_{\gamma^* p}}{\mathrm{d}x\mathrm{d}Q^2\mathrm{d}x_{IP}\mathrm{d}t} = \frac{4\pi\alpha^2_{em}}{xQ^4}\{1-y+\frac{y^2}{2[1+R^{D(4)}(x,Q^2,x_{IP},t)]}\}F_2^{D(4)}(x,Q^2,x_{IP},t), \tag{1.19}$$

where $F_2^{D(4)}$ is is diffractive proton structure function, $R^{D(4)} = (F_2^{D(4)} - 2xF_1^{D(4)})/(2xF_1^{D(4)})$ (due to approximate relation $F_2^{D(4)} \simeq 2xF_1^{D(4)} \to R^{D(4)}$ is typically much smaller than one) and $D(4)$ means diffraction depending on four variables.

In the above formula $R^{D(4)}$ can be neglected, moreover integration over t can be performed. The resulting formula turns out to be

$$\frac{\mathrm{d}\sigma^D_{\gamma^* p}}{\mathrm{d}x\mathrm{d}Q^2\mathrm{d}x_{IP}} = \frac{4\pi\alpha^2_{em}}{xQ^4}\{1-y+\frac{y^2}{2}\}F_2^{D(3)}(x,Q^2,x_{IP}), \tag{1.20}$$

which is analogous to the formula for non-diffractive cross section (1.8) in corresponding variables modified by fractional momentum loss of the proton.

The diffractive structure function $F_2^{D(4)}$ can be also factorised in analogy to the non-diffractive case, so called collinear or hard QCD factorisation [16]

$$\frac{\mathrm{d}F_2^{D(4)}(x,Q^2,x_{IP},t)}{\mathrm{d}x_{IP}\mathrm{d}t} = \sum_i \int_x^{x_{IP}} \mathrm{d}\xi \frac{\mathrm{d}f_i(\xi,\mu_f^2,x_{IP},t)}{\mathrm{d}x_{IP}\mathrm{d}t}\hat{F}_2^i(x/\xi,\mu_f^2), \tag{1.21}$$

where $\mathrm{d}f_i(\xi,\mu_f^2,x_{IP},t)$ is probability density of finding the parton i with momentum fraction ξ in the proton in diffractive regime, μ_f^2 is a factorization scale and $\hat{F}_2^i(x/\xi,\mu_f^2)$ coefficient function calculable in perturbative QCD.

The diffractive proton PDFs can be conveniently expressed in terms of Resolved Pomeron Model [13]. This model assumes that the diffractive parton densities of the proton can be factorised into pomeron flux and pomeron PDFs, so called Regge (or proton vertex) factorisation.

The diffractive parton distribution functions for different values of Q^2 measured by the H1 collaboration are shown in Fig. 1.8. From the figure, it can be deduced that pomeron or diffractive exchange is in general dominated by gluons.

1.4 Photoproduction

The regime of ep collisions in which is Q^2 close to the zero (photon is almost real), where the role of hard scale is taken over by large enough transverse momenta or masses in the HFS is called photoproduction.

The quasi-real photon can interact with proton constituents directly – direct process. Or it can fluctuate into a relatively long living $q\bar{q}$ pair forming partonic state, from which one parton participates in hard scattering – resolved process. Examples of both processes for open charm production are visualized in Fig. 1.9a and 1.9b.

Furthermore considering DIS as a method of investigation of proton partonic structure by virtual photon the photoproduction can be described in reverse way - hard partons from protons are probing the virtual photon. There also exists a consequence of small Q^2 from the experimental point of view – in photoproduction electron/positron changes its direction only slightly and escapes through beam pipe usually undetected.

Direct and resolved processes can be distinguished by variable x_γ (see Fig. 1.9) representing the photon fractional momentum entering the hard subprocess. Naturally in leading order (LO) $x_\gamma = 1$ and $x_\gamma < 1$ for direct and resolved processes, respectively. Also the value of x_γ gives some information about parton which enters the hard subprocess from the photon side. For low values of x_γ the process with gluon is dominant while for high x_γ quarks dominate in the photon.

1.5 Open charm production and D^* mesons

$D^{*\pm}$ is a vector meson containing valence charm quark. The quark content is $c\bar{d}$ for D^{*+} and $\bar{c}d$ for D^{*-}, its mass is (2010.26±0.07) MeV and full decay width (83.4±1.8) keV [18]. The open charm production means that D^* mesons originate from fragmentation of charm quarks. At HERA, the production of charm quarks goes mainly via boson gluon fusion (direct process), but for diffractive photoproduction a non-negligible contribution from resolved process is expected. Leading order diagrams of diffractive open charm production are shown in Fig. 1.9a and 1.9b.

In the presented analysis charm production is tagged by decay products of D^* mesons. In general $D^{*\pm}$ mesons decay by strong and electromagnetic interactions to lighter charmed mesons and then weakly mainly to strange mesons. The decay channel chosen for identification of D^* mesons in further analysis is called golden channel

$$D^{*+} \to D^0\pi^+_{slow} \to (K^-\pi^+)\pi^+_{slow}\ (C.C. \text{ for } D^{*-}) \tag{1.22}$$

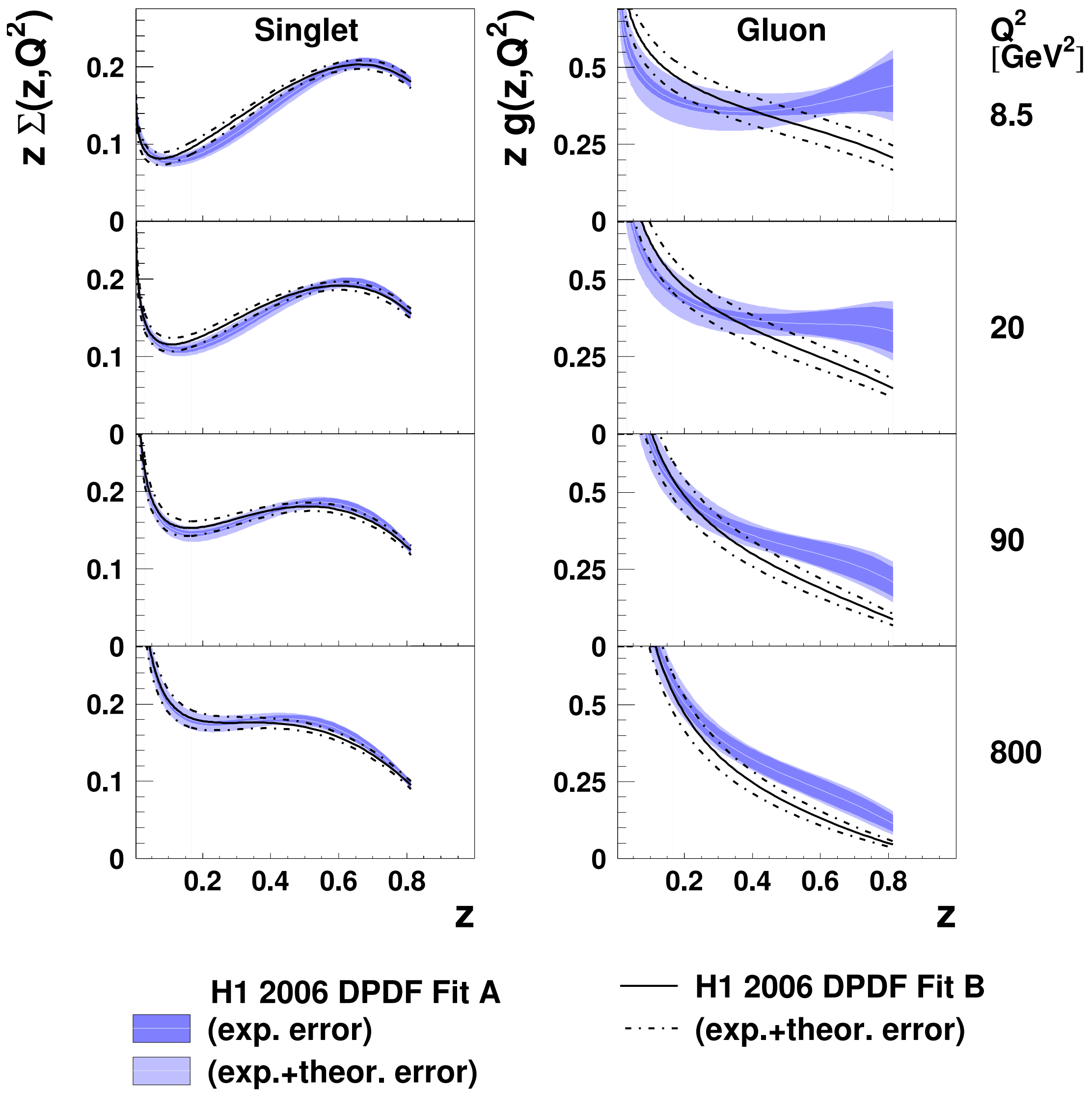

Figure 1.8: The quark singlet ($\Sigma(z, Q^2)$) and gluon ($g(z, Q^2)$) diffractive distribution functions obtained from the H1 2006 DPDF Fit A and the H1 2006 DPDF Fit B in dependence on z. Where $\Sigma(z, Q^2)$ is the quark singlet composed of u, d, s quark and corresponding antiquark distribution functions, which all are considered to be equal. The variable z is the longitudinal momentum fraction of the parton with respect to the pomeron entering the hard subprocess. The diffractive distribution functions are shown for four different values of Q^2 [17].

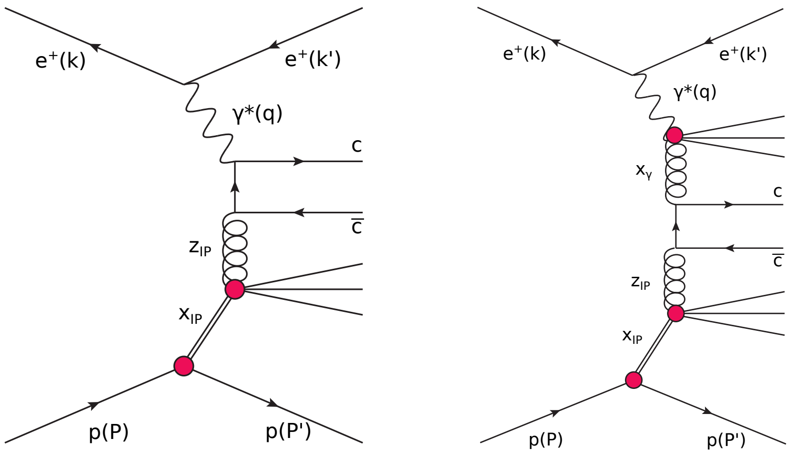

(a) Feynman diagram of direct process (boson-gluon fusion).

(b) Feynman diagram of resolved process.

Figure 1.9: Considered processes for diffractive photoproduction.

which is the easiest channel to study. For the notion of the probability of decay via this channel the branching ratio of the first decay is $(67.7 \pm 0.5)\%$, of the second decay $(3.88 \pm 0.05)\%$ [18]. These data lead to the total probability of decay via golden channel only $\approx 2.6\%$, but still this channel is the most favorable due to presence of small number of only charged tracks which allow us to fully reconstruct the D^* kinematics.

2. Motivation

The presented analysis is supposed to serve as a feasibility study of open charm measurement in the diffractive photoproduction with leading proton detected in the Very Forward Proton Spectrometer (VFPS) [19]. It is a first analysis of this kind in H1. The open charm event candidate tag is provided by a full reconstruction of the D^* meson kinematics decaying via the golden channel. The advantage of the leading proton detection is its experimental complementarity to the previous H1 open charm diffractive photoproduction measurement [20], where the large rapidity gap method was used.

Although the current analysis is based on a data sample of lower luminosity than the previous H1 measurement [20], it benefits from a better performance of charged tracks reconstruction in the studied data period resulting in a larger phase space coverage of D^* kinematics.

The measurement of D^* meson rates in the data, corrected for the influence of detector effects by means of its response simulation, can provide cross section values. A possible comparison with theoretical predictions can provide (within precision of the measurement) information on validity of various theoretical assumptions such as universality of DPDFs, fragmentation model and production mechanism of charm quarks in the above described regime.

There is yet another good reason for this study. It is a well-known suspicion that collinear factorisation (applicability of DPDFs factorised from hard subprocess cross sections) is broken in hard hadron-hadron diffractive scattering [16, 21]. Due to the resemblance of resolved photon interactions with the hadron-hadron ones, one may wonder whether similar effects play a role in the processes of our interest. Both H1 and ZEUS tried to study factorization breaking effects in diffractive photoproduction of dijets in [22, 23, 24, 25], respectively. The H1 and ZEUS came to the different conclusions as concerns observation of the factorisation breaking.

Last but not least the presented analysis, to the extent a diploma work can provide, concludes one of the parts of the original VFPS physics program.

3. Previous results on diffractive open charm photoproduction

The last analysis of diffractive D^* production was published in 2006 and both photoproduction and DIS regimes were included [20]. More details on the methodology can be found in [26]. In [20] the leading proton was not measured, but the large rapidity gap selection method was applied. Therefore the contribution from proton dissociation was present (1.15). Furthermore, the scattered positron was detected in electron tagger in contrast to the presented analysis. The phase space for the measurement can be seen in Table 3.1, where M_Y denotes the mass of proton dissociative system Y.

The reconstruction of D^* candidates was provided using golden decay channel. In the photoproduction regime, the total cross section was measured to be

$$\sigma(ep \to eD^{*\pm}X'Y)_{\gamma p}(\text{data}) = 265 \pm 50(\text{stat.}) \pm 41(\text{syst.})\,\text{pb}. \tag{3.1}$$

Differential cross sections are depicted in Fig. 3.1. The measurement was based on observation of 70 ± 13 measured D^* mesons in total (see Fig. 3.2). For comparison, the NLO QCD calculation using H1 2006 DPDF Fit B predicted

$$\sigma(ep \to eD^{*\pm}X'Y)_{\gamma p}(\text{NLO}) = 359 \pm^{93}_{75}\ \text{pb}, \tag{3.2}$$

which might indicate the non-applicability of collinear factorisation approach.

Hadron level phase space

$M_Y < 1.6\,\text{GeV}$	$\lvert t\rvert < 1\,\text{GeV}^2$	$x_{IP} < 0.04$
$Q^2 < 0.01\,\text{GeV}^2$	$0.3 < y < 0.65$	
$p_t(D^*) > 2\,\text{GeV}$	$\lvert\eta(D^*)\rvert < 1.5$	

Table 3.1: The hadron level phase space definition in previous analysis [20].

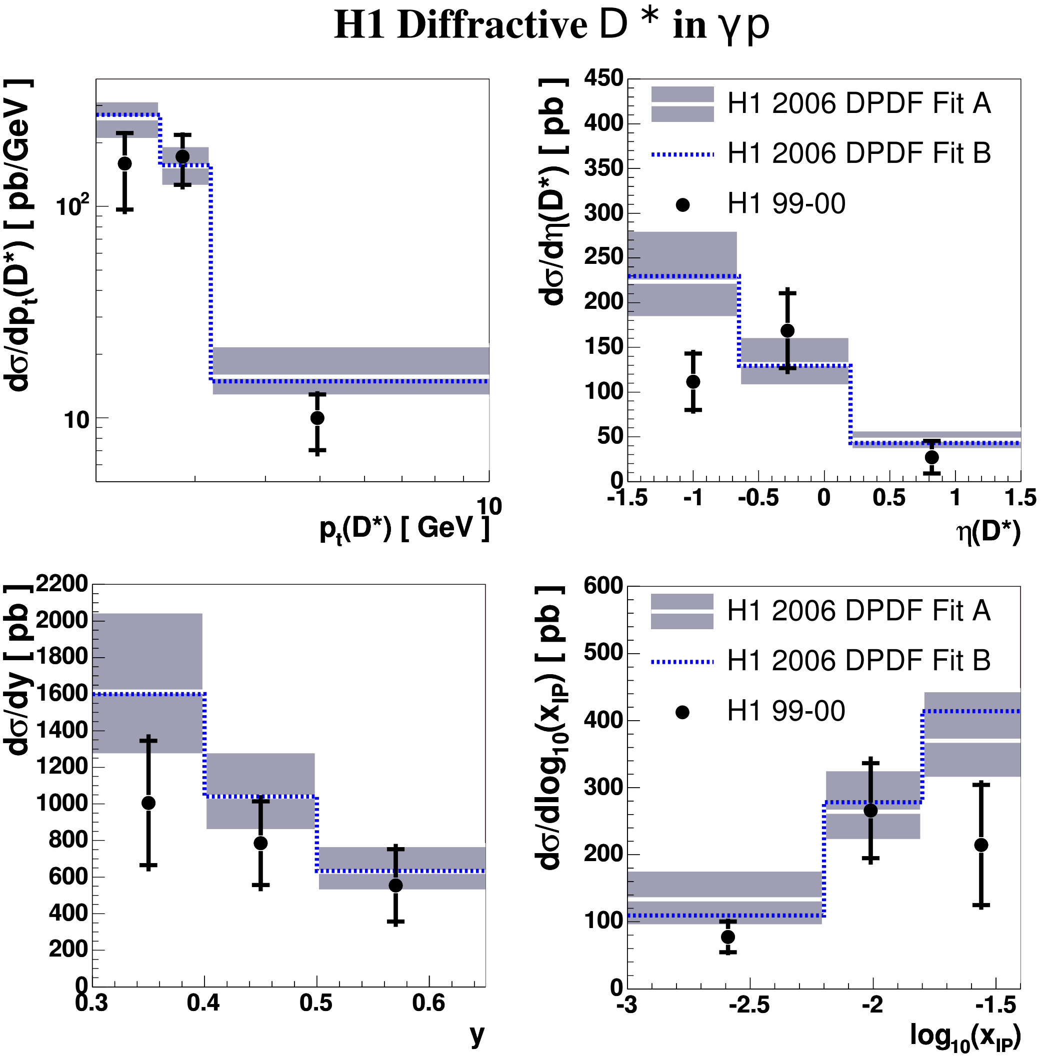

Figure 3.1: The cross sections of diffractive D^* photoproduction differential in $p_t(D^*)$, $\eta(D^*)$, y and $\log x_{IP}$. The measured data are compared with NLO QCD calculations [20].

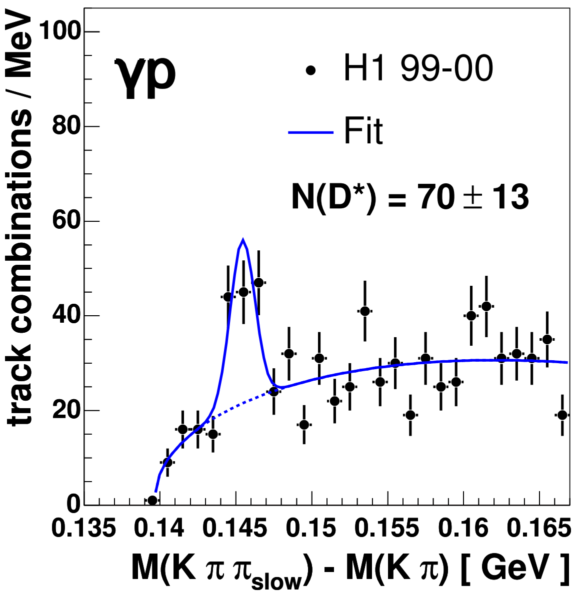

Figure 3.2: Fit of D^* candidates distribution in $m(D^*) - m(D^0)$ [20].

4. HERA and H1

4.1 HERA accelerator

HERA (Hadron-Elektron Ring Anlage) was the only existing electron (positron) proton ring collider located at the research center DESY (Deutsches Elektronen Synchrotron) in Hamburg, Germany (see Fig. 4.1) designed to investigate the structure of proton and consequently test QCD, search for new phenomena and much more. This "huge electron microscope for viewing the structure of protons" started to operate in 1992 when the first collisions begun to be examined by 4 experiments located at 4 interaction points along the HERA. The mentioned experiments were two universal – H1 and ZEUS and two fixed target – HERMES and HERA-B.

Protons and electrons were accelerated separately in a tunnel with circumference 6.3 km, roughly 25 meters under the ground. Collisions of bunches of protons with energy up to 920 GeV and electrons (positrons) with energy 27.6 GeV took place every 96 ns in the interaction points. HERA operated as "HERA-I" from 1992 to 2000. After this phase HERA underwent an upgrade, when the proton energy was increased from initial 820 GeV to 920 GeV, the experiments were upgraded and the luminosity was improved. The integrated luminosity over the years of HERA operation can be seen in Fig. 4.2, for HERA-I it is roughly 130 pb^{-1}, for HERA-II 360 pb^{-1}.

4.2 H1 experiment

The H1 experiment was located in the north hall of HERA and was designed to investigate multiple aspects of electron-proton scattering. So H1 was able to detect both hadrons and leptons in nearly full solid angle. The H1 detector, shown in Fig. 4.3, was asymmetric, due to the higher energy of the proton and was constructed from number of sub-detectors which will be briefly described.

Charged particles were tracked using trackers, which consisted of drift chambers, proportional chambers and silicon trackers. The device for measuring the energy of particles was liquid argon calorimeter (LAr) covering angular range $4^\circ < \Theta < 154^\circ$. This calorimeter had two parts - electromagnetic and hadronic. Although the interaction medium remained the same, the absorbers for both parts differed. In electromagnetic calorimeter case, the absorber was made of lead, in hadronic from steel. Final energy resolution for the electromagnetic calorimeter was $\sigma(E)/E = 11\%/\sqrt{E/\mathrm{GeV}} \oplus 1\%$. Achieved resolution for the hadronic calorimeter was $\sigma(E)/E = 50\%/\sqrt{E/\mathrm{GeV}} \oplus 2\%$. Measurement in a backward region was provided by the SpaCal calorimeter which was constructed from scintillating fibers laid in the lead and was also divided into hadronic and electromagnetic parts. Other parts of the H1 were forward detectors (PLUG, FMD, FTS, ...) and muon detectors, for detailed information see [27].

The luminosity at HERA was determined with utilization of well known Bethe-Heitler Bremsstrahlung [28] process

$$ep \to ep\gamma, \tag{4.1}$$

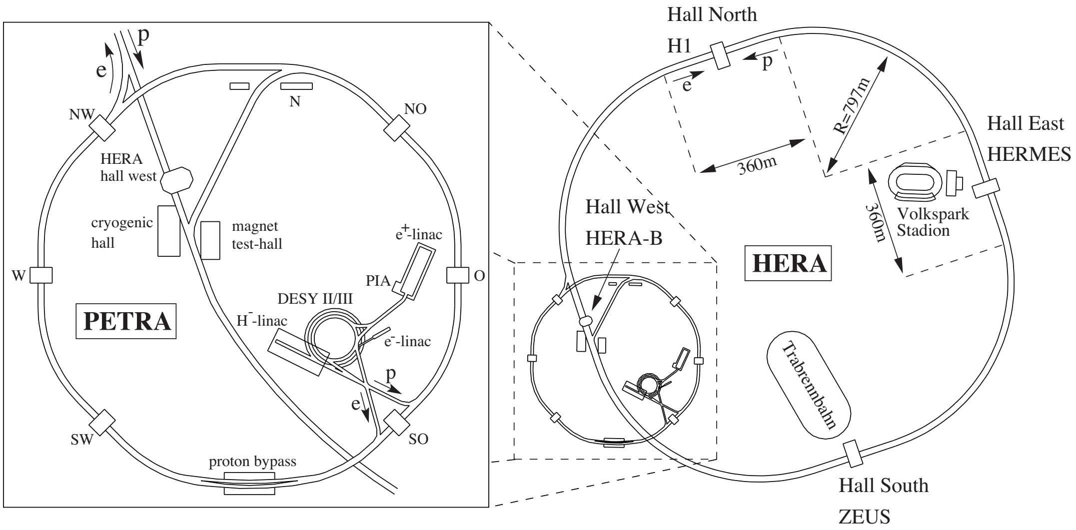

Figure 4.1: The HERA accelerator.

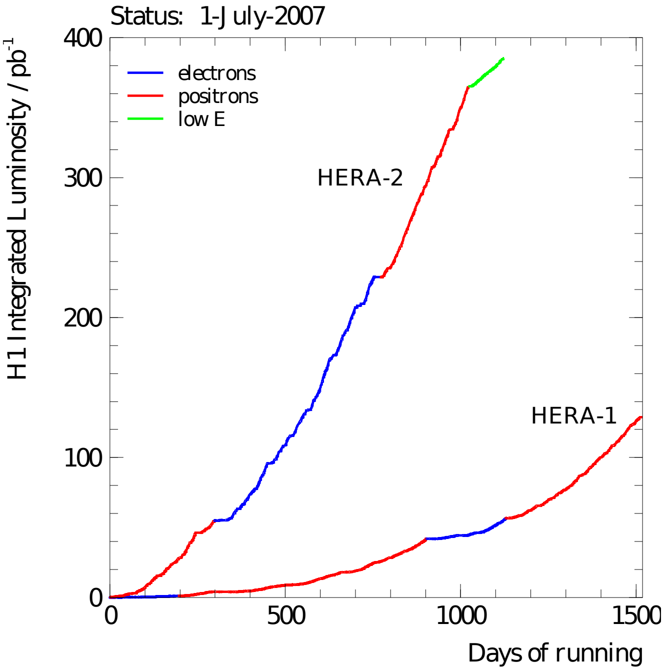

Figure 4.2: Integrated luminosity of H1 experiment as a function of days of running from start of HERA-I and HERA-II operation.

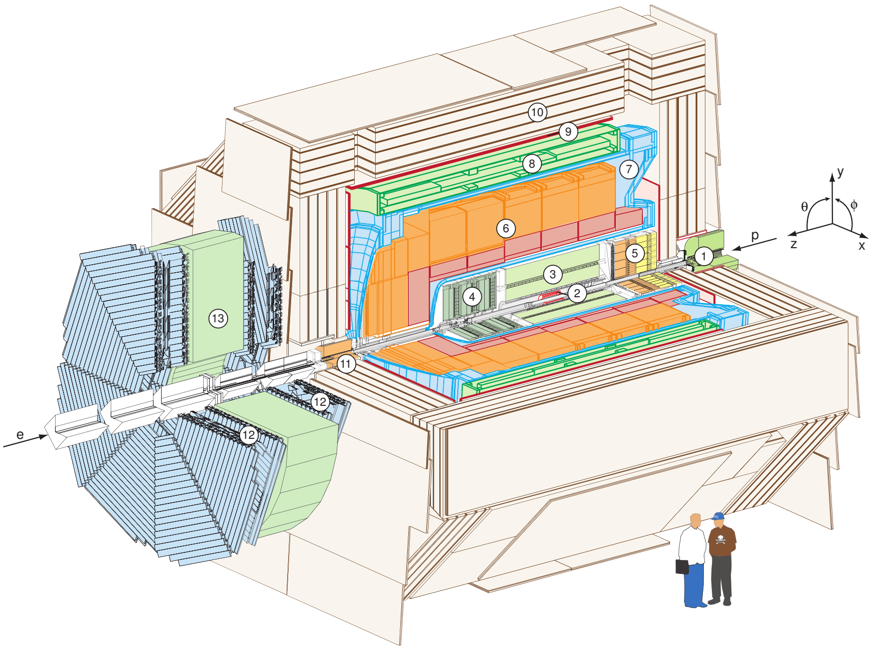

① Beam pipe and beam magnets
② Silicon tracking detector
③ Central tracking detector
④ Forward tracking detector
⑤ Spacal calorimeter (em and had)
⑥ Liquid Argon calorimeter (em and had)
⑦ Liquid Argon cryostat
⑧ Superconductiong coil
⑨ Muon chambers
⑩ Instrumented iron (streamer tube detectors)
⑪ Plug calorimeter
⑫ Forward muon detector
⑬ Muon toroid magnet

Figure 4.3: Schematic view of the H1 detector. The definition of the coordinate system used in this thesis is given on the right side of the figure. The x-axis points to the center of the HERA ring.

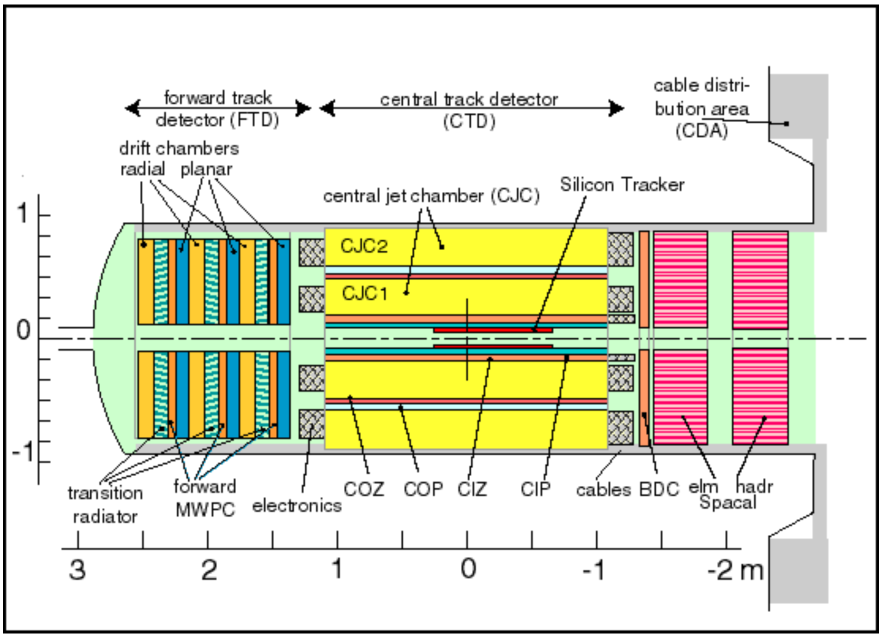

Figure 4.4: Schema of the H1 tracking system.

which can be precisely calculated within the perturbative QED. In H1 the scattered electron and γ were directly detected by dedicated detectors.

Knowing the total cross section σ and measuring the event rate N of this process the luminosity $\mathcal{L}$ is then calculable as

$$\mathcal{L} = \frac{N}{\sigma}. \tag{4.2}$$

4.2.1 H1 trackers

The H1 tracking system was designed for triggering, particle reconstruction and identification. The tracking system can be divided into forward (FTD) $7^\circ < \Theta < 25^\circ$ and central (CTD) $15^\circ < \Theta < 165^\circ$ tracking devices. Due to HERA *ep* collisions asymmetry these parts were very different. The tracking system is depicted in Fig. 4.4.

The main parts of the CTD were two drift chambers CJC1 and CJC2. These drift chambers contained wires parallel to the beam axis. Further smaller drift chambers CIZ and COZ with wires perpendicular to the beam axis were also components of the central tracking system. The triggering was ensured by the multiwire proportional chambers namely the central inner proportional chambers (CIP), the central outer proportional chamber (COP) and the forward proportional chambers (FWPC) [29].

The FTD was actually never used in analyses due to the operational problems.

4.3 Very Forward Proton Spectrometer

Following analysis uses data obtained from Very Forward Proton Spectrometer (VFPS) [19] measurements, thus this device will be discussed in more detail

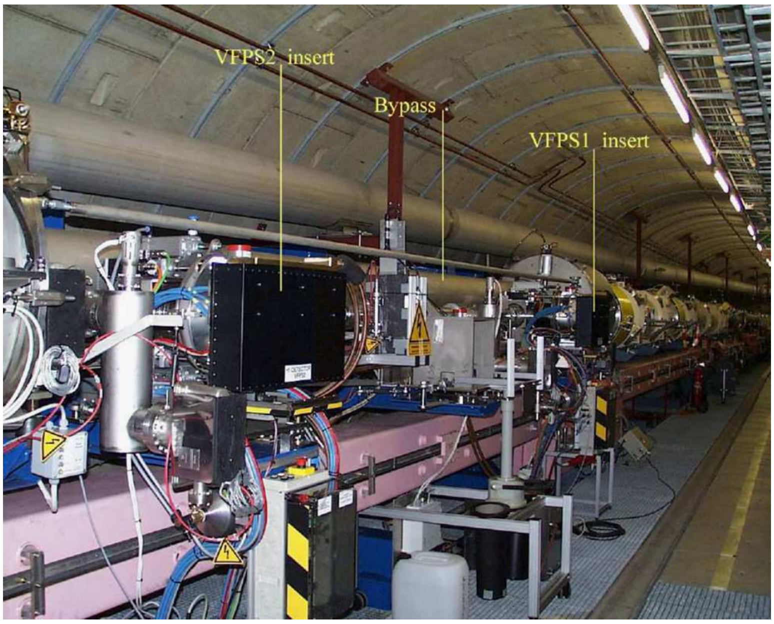

Figure 4.5: Very Forward Proton Spectrometer at HERA [19].

in this section. VFPS was a component of the H1 detector and was designed to complement the existing Forward Proton Spectrometer (FPS). VFPS was installed in 2006 and its aim was to measure the scattered protons from diffractive processes and to extend the acceptance coverage in comparison with FPS.

4.3.1 VFPS description

VFPS detector was composed of two sub-detectors VFPS1 and VFPS2 located at 218 m (VFPS1) and 222 m (VFPS2) from the interaction point. The possible positions were found to be only in the cryogenic sections of HERA at drift spaces at the positions 195 m, 190 m and 220 m. The best acceptance in x_{IP} and t was found to be at 220 m [30]. Additionally in the cryogenic section no access to the beam was possible, so "cryogenic bypass" had to be constructed. The setup at 220 m is shown in Fig. 4.5.

The VFPS detectors were located in separate horizontal Roman pot stations in order to be able to move towards and away from the proton beam. During injection and ramping of the beams the VFPS detectors used to rest in parking positions and only when the beam was stable they moved close to the beam. The movement was realized by a stepper motor, nevertheless the position of the detector was not obtained from the motor step size but from an external measurement device. Each VFPS station was equipped with two scintillating fiber detectors separated by 60 mm along the beam direction. Each fiber detector consisted of two layers of perpendicularly oriented fibers (±45° with respect to the vertical direction). Every fiber layer was made of five rows of staggered fibers (120 fibers per row). The fiber diameter was 480 μm. The signal from scintillating fibers was led to the position-sensitive photomultipliers. Every detector was sandwiched in scintillating tiles, which operated as detector trigger. Schema of VFPS is shown in Fig. 4.6, actually the VFPS detector design was derived from FPS. More details

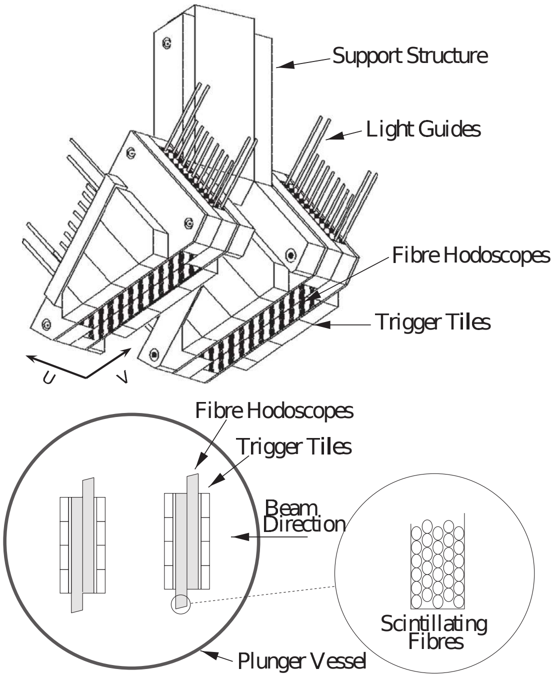

Figure 4.6: VFPS station detector schema [19].

about VFPS can be found in [19].

Scattered protons with fraction of momentum $1 - x_{IP}$ in range $0.008 < x_{IP} < 0.028$ and $|t| < 0.5\,\mathrm{GeV}^2$ could be measured by the VFPS detector. Data collected by VFPS can be divided into two periods. In the first period from 2005 until June 2006 e^-p data were gathered, in the second period from June 2006 to March 2007 were accelerated positrons instead of electrons. The total integrated luminosity of the second period was $130\,\mathrm{pb}^{-1}$. The integrated luminosity of VFPS compared to the H1 luminosity can be seen in Fig. 4.7. The difference in luminosity collected by H1 alone and while using VFPS is given by the time needed to insert/retract the detectors. Over both periods energy of incoming protons was 920 GeV and electrons/positrons 27.6 GeV.

4.3.2 VFPS tracks and reconstruction of diffractive kinematics

In both VFPS stations local tracks were reconstructed separately and then combined to the global track specifying the position (x, y) and angle (x', y') halfway between VFPS stations. These data were used to reconstruct diffractive proton fractional momentum loss x_{IP} and emission angles Θ_x, Θ_y. But first the passage of diffractive proton through the beam optics from H1 to VFPS had to be simulated. The simulation was implemented in two ways. As a standalone program and complexly as a part of H1SIM (based on GEANT) including a complete description of the geometry. From the simulated events' tracks, the diffractive proton parameters $(x_{IP}, \Theta_x, \Theta_y)$ in the primary vertex could be linked with parameters measured by the VFPS. The correlation of coordinate x/y and angle x'/y' in the middle between VFPS stations and the diffractive proton variables $x_{IP}, \Theta_x, \Theta_y$ is shown in Fig. 4.8. For illustration in Fig. 4.9 the horizontal and vertical positions

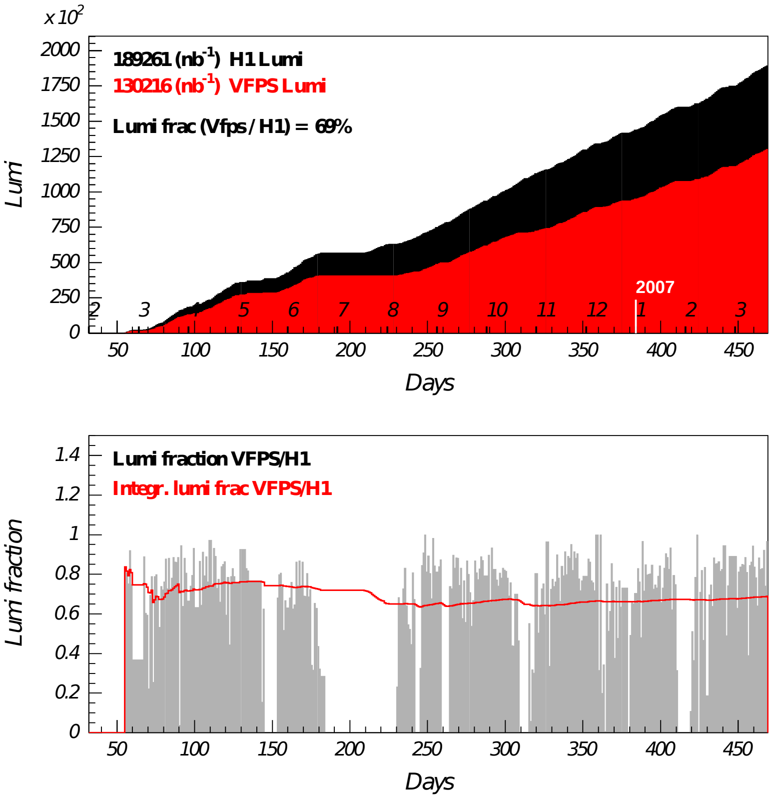

Figure 4.7: In the top figure is cumulative integrated luminosity registered by H1 and VFPS as a function of the days from the start of VFPS operation, on the bottom luminosity fraction VFPS/H1 [19].

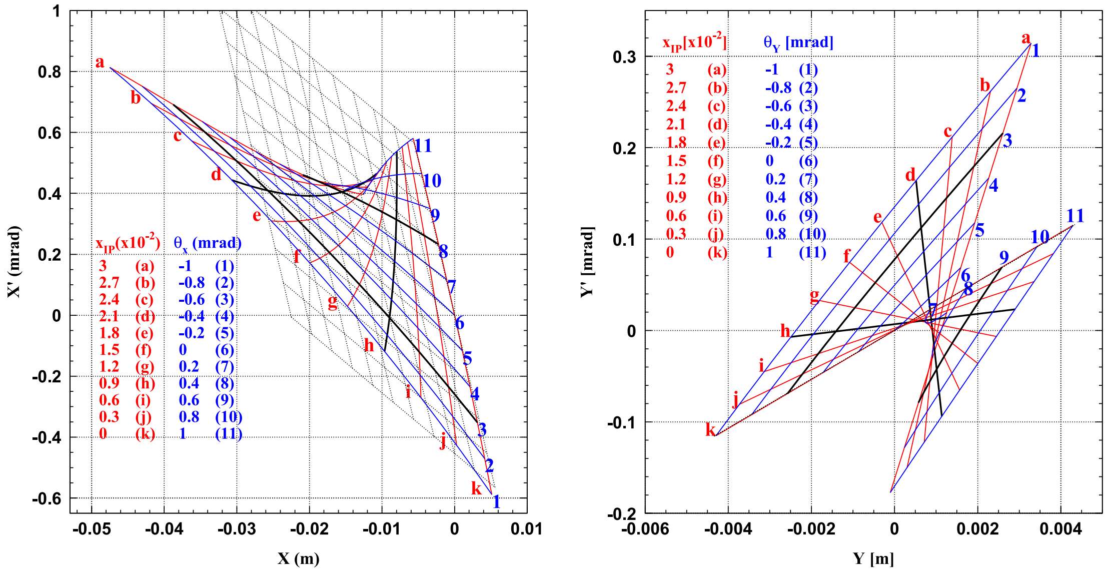

Figure 4.8: Correlation of (x, x') and (y, y') coordinates in the middle between the stations for protons with certain values of $(x_{IP}, \Theta_x, \Theta_y)$ in interaction point (blue and red lines). The grey net represents the same correlation for the linear beam optics [19].

of diffractive protons are plotted for fixed $x_{IP} = 0.02$ and several values of t.

Important task was to link coordinates (x, y) and (x', y') with diffractive proton parameters $(x_{IP}, \Theta_x, \Theta_y)$ in the interaction point. For this purpose, neural network method trained at simulated events was applied. The task of the proton diffractive kinematics reconstruction is complicated due to the fact that the transport matrix of beam optics depends on the four-momentum of the proton because of non-linear beam optics effects.

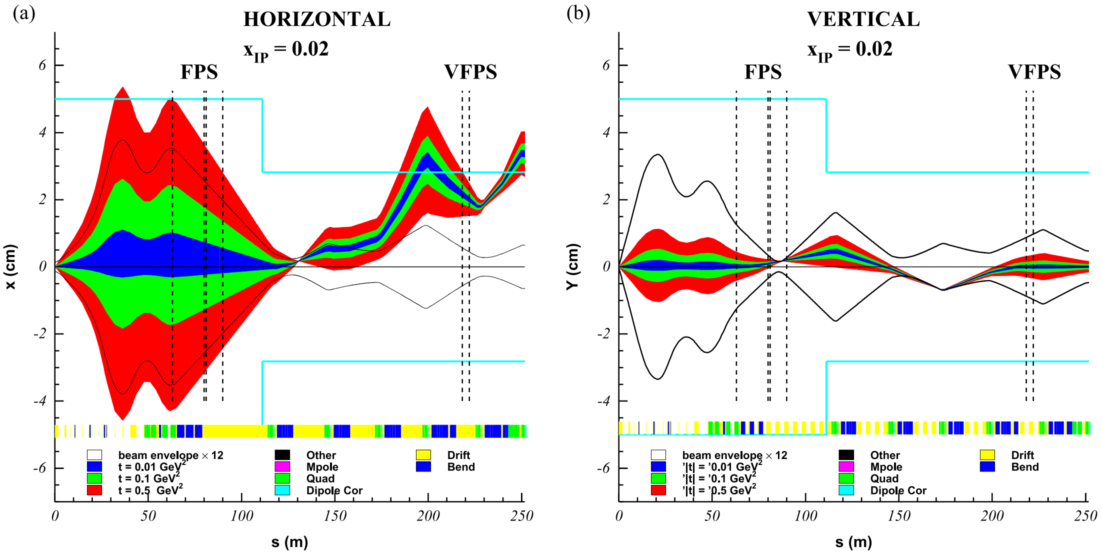

Figure 4.9: The x and y projection of the beam envelope as a function of distance. The blank area represents the 12σ beam envelope and the coloured regions represent the x and y projections of diffractive protons for fixed value of $x_{IP} = 0.02$ and different values of $|t|$. The beam pipe is shown in light blue color, the colored areas at the bottom of figures indicate magnet elements and drift spaces. The vertical dashed lines represent the positions of FPS and VFPS stations [19].

5. Diffraction detection methods

5.1 Rapidity gap method

Diffractive scattering $ep \to eXp$ is characteristic for the presence of rapidity gaps. Due to a colorless character of diffractive exchange, proton and the system X do hadronize independently. Thus, diffractive events can be recognized by the presence of a gap in hadronic activity in the forward region. The typical diffractive photoproduction event as seen in H1 detector is depicted in Fig. 5.1.

The rapidity y is defined as

$$y = \frac{1}{2} \ln \left(\frac{E + p_z}{E - p_z} \right), \tag{5.1}$$

where E denotes an energy of the particle and p_z its z-component of momentum. Experimentally more convenient is variable called pseudorapidity η, which can be introduced as follows

$$\eta = -\ln \left[\tan \left(\frac{\Theta}{2} \right) \right], \tag{5.2}$$

where Θ is the angle with respect to the beam axis. For massless and very relativistic particles rapidity and pseudorapidity coincide.

In H1, the pseudorapidity of the most forward calorimeter energy deposition is used as a variable sensitive to the rapidity gap size. The advantage of this method is that it gives a reasonably high statistics and only the standard and well-understood parts of the H1 detector are needed. Its unpleasant disadvantage is the background from proton dissociation and non-diffractive processes. This method is the most often used one in H1.

5.2 Leading proton tagging

In diffraction, the scattered proton escapes through the beam pipe because its direction is changed only slightly. Thus spectrometers FPS and VFPS were installed with the aim to detect the leading proton. VFPS was the successor of the FPS measuring in a different diffractive kinematic region. The VFPS detector used in this analysis is described in a more detailed way in Sec. 4.3.

In general the Roman pots with the detectors cannot move arbitrarily close to the beam what results in a certain limitation in the acceptance. Nonetheless, the kinematics of diffractive proton can be determined more precisely in comparison with reconstruction relying on the properties of the hadronic final state (measured in the central detector only).

The advantages of using proton spectrometers are obvious. Due to the direct measurement of the leading proton no dissociation is present and background from non-diffractive processes is in measurements using VFPS smaller than 1%. Further, the kinematics of leading proton is reconstructed much more accurately and contrary to the LRG method also t variable can be determined. On the other hand, the proton tagging is experimentally very demanding. Also the reconstruction of the kinematic variables is complicated because the leading proton passes through the non-linear accelerator optics.

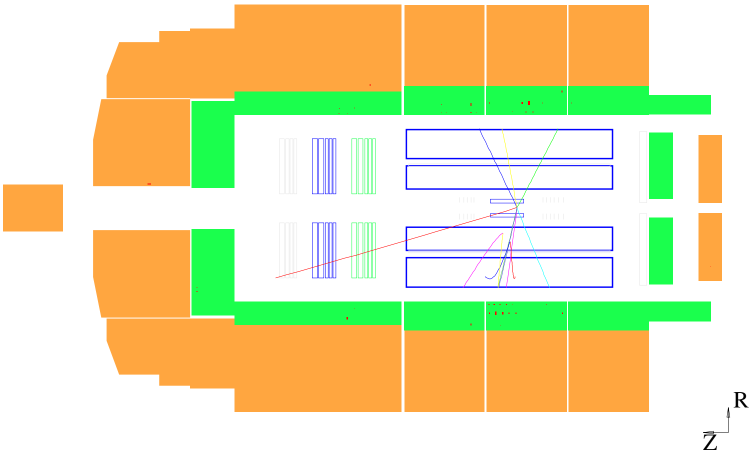

Figure 5.1: Diffractive photoproduction event as seen in the H1 detector.

6. Events generation and simulation

6.1 Leading-order Monte Carlo generators

Monte Carlo (MC) programs are widely used to generate particle collisions according to given physics model. The generation of an event can be divided into few steps: hard process, parton showers, hadronization and unstable particles decays [31]. The hard process describes scattering between two partons and is calculated by the means of perturbation theory. The incoming and outgoing quarks and gluons are colored, so they can radiate and produce parton showers. The final state parton shower evolves until perturbation theory breaks down and the further evolution must be described by a hadronization model. The hadronization model covers the transition from colored objects into colorless observable hadrons.

6.1.1 MC generator Rapgap

The provided analysis uses the MC generator Rapgap for the events generation. Rapgap is LO MC model, which was created to describe diffractive/non-diffractive DIS and diffractive photoproduction [32].

The use of Monte Carlo generator is twofold, it can provide predictions for physics processes but also it can serve as an input to a detailed simulation of detector response, therefore the simulated MC events provide a tool to correct the measured data for the detector effects. For the purpose of this analysis large sample of MC events was generated with MC Rapgap using H1 2006 DPDF Fit B for the direct and resolved γ photoproduction.

In general the included hard sub-processes in MC Rapgap are

$$eq \rightarrow e'q' \; (+\text{C.C.}), \tag{6.1}$$

$$eq \rightarrow e'qg \; (+\text{C.C.}), \tag{6.2}$$

$$eg \rightarrow e'q\bar{q}, \tag{6.3}$$

$$\gamma q \rightarrow qg \; (+\text{C.C.}), \tag{6.4}$$

$$\gamma g \rightarrow q\bar{q}, \tag{6.5}$$

$$gg \rightarrow gg, \tag{6.6}$$

$$qg \rightarrow qg \; (+\text{C.C.}), \tag{6.7}$$

$$q\bar{q} \rightarrow gg, \tag{6.8}$$

$$q\bar{q} \rightarrow q\bar{q} \tag{6.9}$$

and

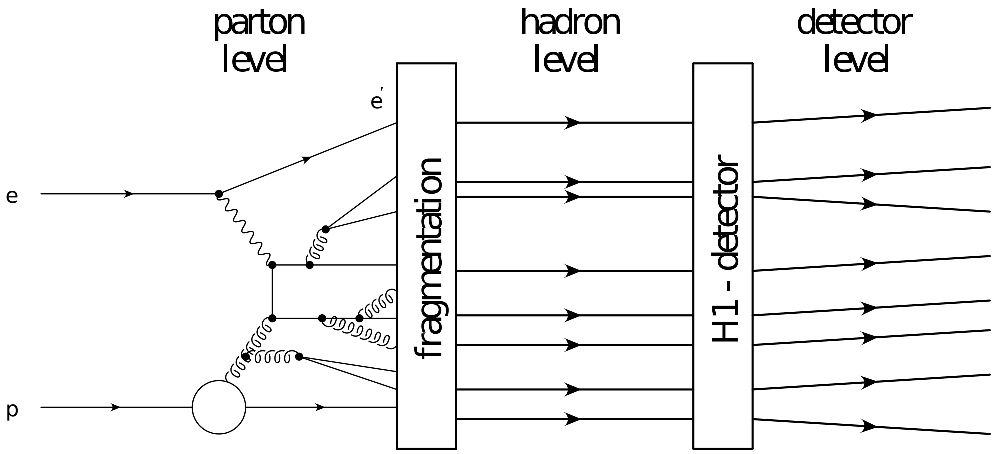

Figure 6.1: Schema of MC generation and simulation of event.

$$qq \to qq\ (+\text{C.C.}). \tag{6.10}$$

Thus RAPGAP is capable to describe both direct and resolved processes in photoproduction if photon parton distribution function (GRV in the case of this analysis [33]) is provided for the later one. These processes are calculated only in LO QCD, but additionally the initial and final state parton showers which can mimic to some extent the effects of higher orders are switched on. The hadronisation in RAPGAP is provided using the phenomenological Lund string model [34].

6.2 Detector response simulation

The simulation of the detector response is provided by the GEANT program [35]. After the precise description of the detector is given to GEANT, the Monte Carlo generated events are processed and the detector response is simulated. The elementary schema of event generation and simulation is given in Fig. 6.1.

6.3 Correlation of the detector-hadron level

In this section, the correlations between hadron (true) and detector level observables are shown. These correlations are presented as scatter plots in desired kinematic variables on both levels. Further the relative resolutions representing the D^* candidates distribution in $\frac{x^{detector} - x^{true}}{x^{true}}$, where x denotes arbitrary variable, are also shown. From these plots, the quality of reconstruction can be deduced.

The correlation plots between the detector level variables $\eta(D^*)$, $p_t(D^*)$, y_h, x_{IP}^{H1} and x_{IP}^{VFPS} and corresponding variables on the hadron level are shown in Fig. 6.2, 6.3, 6.4, 6.5 and 6.6. The variables y_h and x_{IP}^{H1} were reconstructed from hadronic final state X measured in H1 detector. Conversely the variable x_{IP}^{VFPS} was obtained from leading proton measurement in VFPS. From the mentioned scatter plots a good reconstruction of D^* meson p_t and η is visible. On the other hand variables y_h and x_{IP}^{H1} calculated from hadronic final state are reconstructed rather poorly – for both the correlation gets worse for increasing y_h and x_{IP}^{H1}. As

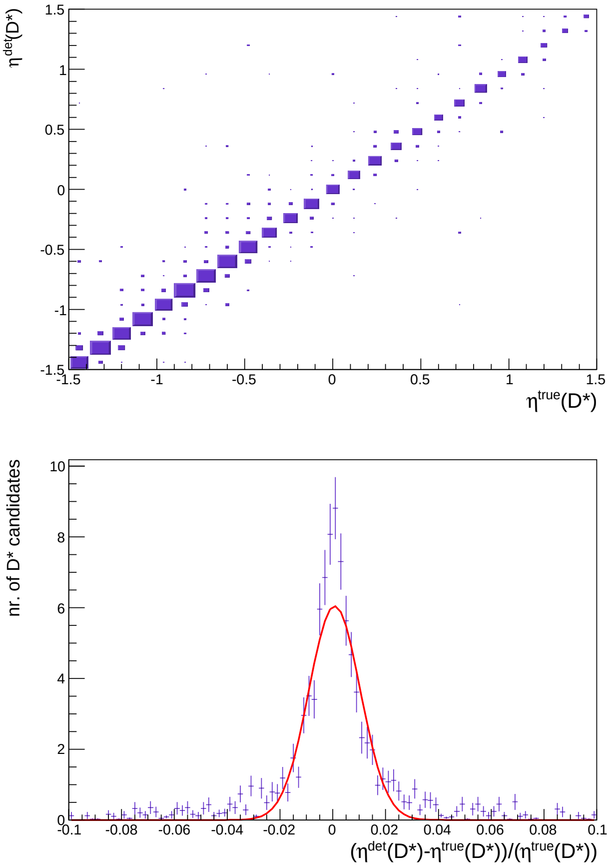

Figure 6.2: Correlation of $\eta(D^*)$ between the hadron and detector level. The areas of the rectangles are proportional to the event rates in the corresponding kinematic region. In addition, the relative resolution fitted by Gaussian function is shown.

it can be seen from the figure 6.6 the correlation of x_{IP}^{VFPS} with the true value of x_{IP} is significantly better.

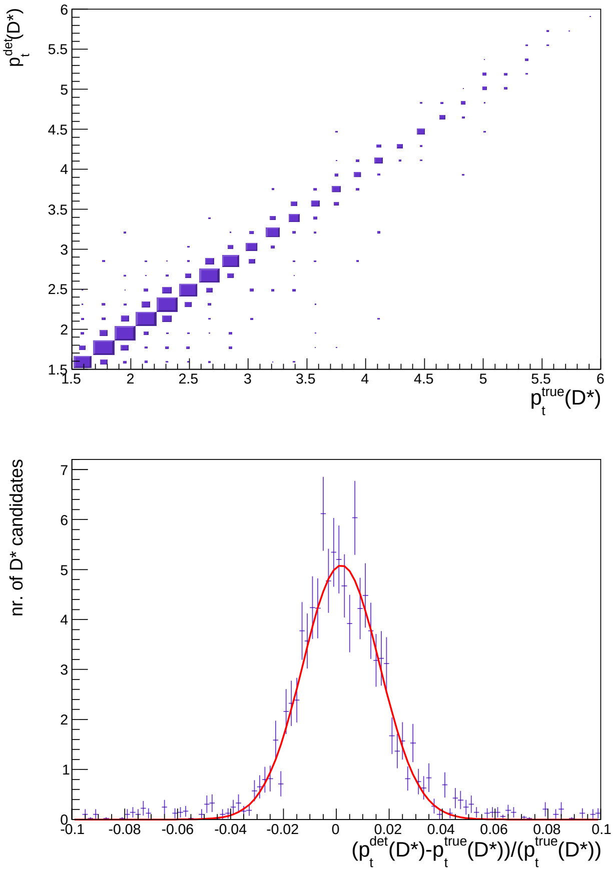

Figure 6.3: Correlation of $p_t(D^*)$ between the hadron and detector level. The areas of the rectangles are proportional to the event rates in the corresponding kinematic region. In addition, the relative resolution fitted by Gaussian function is shown.

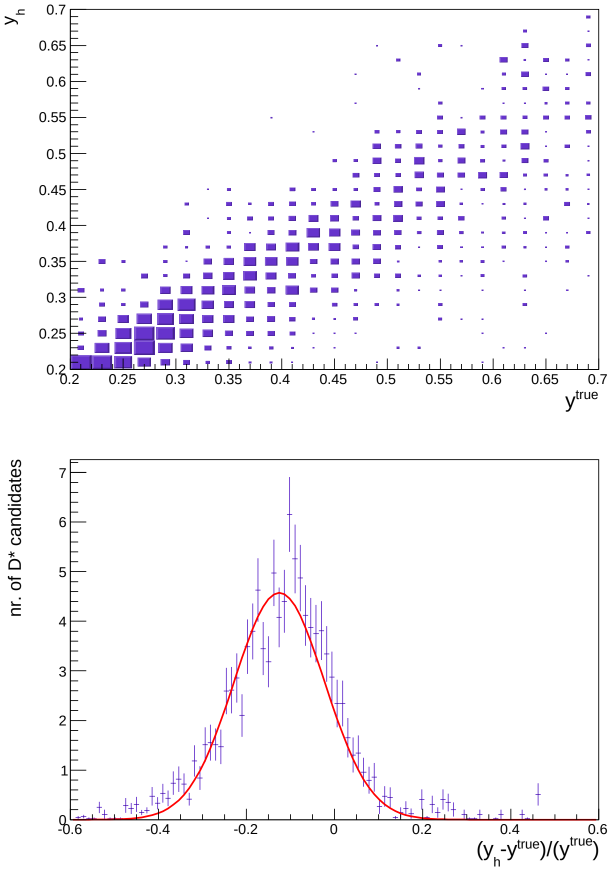

Figure 6.4: Correlation of y_h between the hadron and detector level. The areas of the rectangles are proportional to the event rates in the corresponding kinematic region. In addition, the relative resolution fitted by Gaussian function is shown.

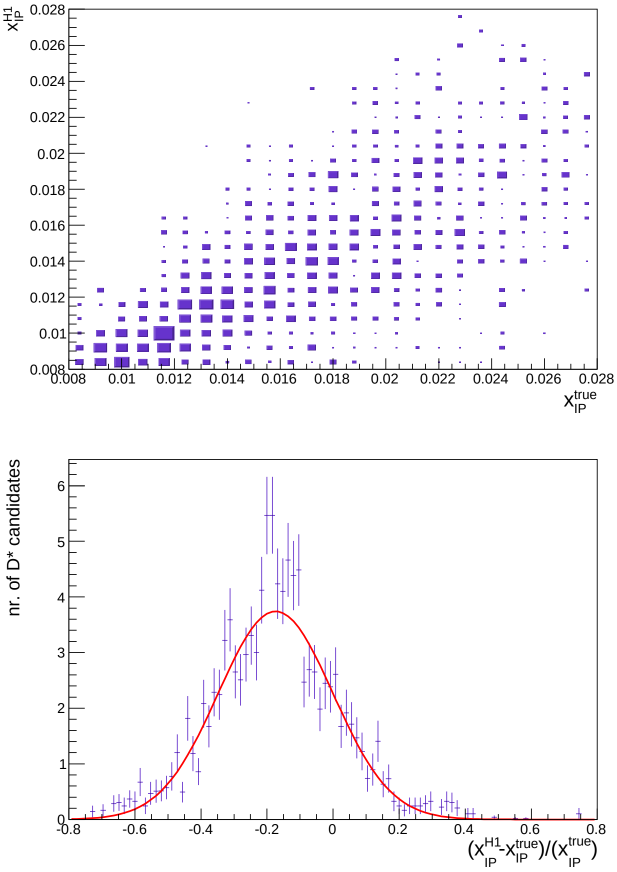

Figure 6.5: Correlation of x_{IP} between the hadron and detector level. On the detector level x_{IP} was obtained from the hadronic final state X. The areas of the rectangles are proportional to the event rates in the corresponding kinematic region. In addition, the relative resolution fitted by Gaussian function is shown.

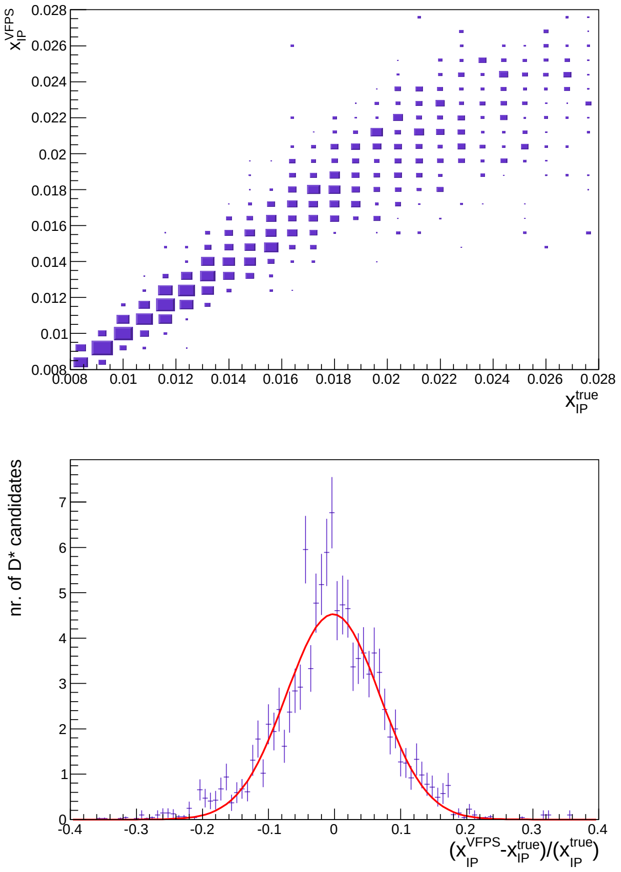

Figure 6.6: Correlation of x_{IP} between the hadron and detector level. On the detector level x_{IP} was obtained from the VFPS measurements. The areas of the rectangles are proportional to the event rates in the corresponding kinematic region. In addition, the relative resolution fitted by Gaussian function is shown.

7. Run and event selection

This analysis is to the large extent based on data and several MC samples used in the analysis of diffractive dijet photoproduction [24]. Also the non-trivial part of the analysis such as determination of trigger efficiency and optimization of quality cuts ensuring the reliable VFPS measurement was adopted from this analysis.

7.1 Data samples

The diffractive photoproduction data were taken from 17-Oct-2006 to 03-Mar-2007 corresponding to integrated luminosity $30.2\,\mathrm{pb}^{-1}$.

7.2 MC samples

The analysis used Boson-Gluon Fusion BGF (uds, c), QCDC (uds), resolved γ (uds) MC samples for both pomeron and reggeon. Later the discrepancy between number of D^* mesons in data and simulation led to the need of new MC samples. The BGF (c) and new resolved γ (uds, c) samples were generated and simulated with higher statistics. Eventually in the presented D^* analysis only the signal charm BGF (c) and resolved γ (uds, c) MCs are used.

7.3 Event selection

To preselect the events for this analysis, the subtrigger $S103$ with efficiency around 80% was used. Basic requirements for diffractive photoproduction events were the presence of the diffractive proton in the VFPS, reconstructed primary vertex and missing positron candidate. To choose good events measured by the VFPS the signal in the VFPS meaning the local tracks in both VFPS1 and VFPS2 stations must exist. The VFPS trigger condition is that at least one tile per trigger plane has to fire and three out of four trigger planes must fire in each VFPS station. Moreover event's local tracks geometrically consistent to form a global track are required. The VFPS had a limited acceptance in x_{IP} and t variables, so this fact has to be also taken into the account. List of VFPS conditions is shown in Tab. 7.1.

Further, the photoproduction regime is pursued and the reliable data reconstruction is required. The primary vertex must be found (`IvTyp` $= 1$). To ensure a satisfactory measurement precision the z-vertex and y_h reconstructed from the hadronic final state must be within the specific interval. The photoproduction cuts are summarized in Tab. 7.2.

Another set of cuts is needed in order to restrict background. The cut for x_{IP}^{H1} helps to suppress the background from the beam halo in VFPS. In addition, such background events are significant for small proton energy loss, not comparable with the energy loss measured by the H1 detector. For the VFPS and H1 setup the cuts introduced in Tab. 7.3 are required [24].

VFPS selection	
`VFPS1te`	$= 1$
`VFPS2te`	$= 1$
`JTSTc_VFPS1_nr`	$= 1$
`JTSTc_VFPS2_nr`	$= 1$
`JTGTc_nr`	$= 1$
$\|t\|$	< 0.5 GeV^2
x_{IP}^{VFPS}	> 0.008
x_{IP}^{VFPS}	< 0.028

Table 7.1: VFPS measurement requirements.

Photoproduction selection	
`IvTyp`	$= 1$
$\|z_{Vtx}\|$	< 30 cm
y_h	> 0.2
y_h	< 0.7
No positron candidate	

Table 7.2: Selection for photoproduction and reliable data.

Background restriction	
x_{IP}^{H1}	< 0.04
$x_{IP}^{VFPS}/x_{IP}^{H1}$	> 0.6
VFPS fiducial cuts	

Table 7.3: Selection in order to restrict background.

D^* **selection**	
$p_t(K)$	> 0.3 GeV
$p_t(\pi)$	> 0.3 GeV
$p_t(\pi_{slow})$	> 0.12 GeV
$p_t(K) + p_t(\pi)$	> 2 GeV
$\lvert m(D^0) - m(K\pi)\rvert$	< 0.08 GeV
$\Delta m = m(D^*) - m(D^0)$	< 0.170 GeV
$p_t(D^*)$	> 1.5 GeV
$\lvert\eta(D^*)\rvert$	< 1.5

Table 7.4: D^* candidate tracks selection.

Hadron level selection	
Q^2	< 2 GeV^2
$p_t(D^*)$	> 1.5 GeV
$\lvert\eta(D^*)\rvert$	< 1.5
y	> 0.2
y	< 0.7
x_{IP}	> 0.008
x_{IP}	< 0.028
$\lvert t\rvert$	< 0.5 GeV^2

Table 7.5: The hadron level phase space definition.

Finally, the request is to select only the D^* candidates. The transverse momenta of the decay products are required to be above a certain limit to ensure satisfactory track reconstruction. The efficient η region is provided by the η cut on the D^* candidates. The aim of cuts is also to suppress the background. Cuts used to select D^* candidates in the golden decay channel are presented in Tab. 7.4.

On the hadron level, the D^* decaying through golden channel is required. The hadron level phase space for this analysis is defined in Tab. 7.5.

7.4 Reconstruction formulae

In the photoproduction regime, the electron changes its direction only slightly so it can be measured only by dedicated electron taggers – what is not the case of this analysis. The electron is not tagged and escapes through the beam pipe. Thus, all kinematic variables have to be determined from the hadronic final state and the leading proton which is tagged in VFPS. The y_h and x_{IP}^{H1} variables can be determined from HFS as follows

$$x_{IP}^{H1} = \frac{\sum_i (E_i + p_{z,i})}{2E_p}, \tag{7.1}$$

$$y_h = \frac{\sum_i (E_i - p_{z,i})}{2E_e}, \tag{7.2}$$

where i runs over the particles in hadronic final state, E_p and E_e are energies of incoming proton and electron, E_i and $p_{z,i}$ energy and z-component of momentum of particle i from HFS.

As it was already said x_{IP}^{VFPS} was determined from the VFPS measurement (x, y, x', y') using the neural network method.

8. Signal extraction

The kinematics of the D^* golden channel decay products provides rather stringent restrictions on tracks seen in the detector. The fact, that D^* decays firstly to D^0 and pion also constraints the kinematics of the D^0 decay products. The convenient variable to look at is the difference of invariant masses of the D^* and D^0 candidates tracks. Furthermore, the difference between the D^* and D^0 mass (145.421 ± 0.010) MeV [18] which is slightly above the charged pion mass implies that the pion from the $D^{*\pm} \to D^0\pi^\pm$ is rather slow in the rest frame of the D^* meson. That is why the golden channel is often written as $D^{*\pm} \to K^\mp\pi^\pm\pi^\pm_{slow}$, where $\pi^\pm_{slow}$ denotes the slow pion. Finally, the variable used to distinguish D^* mesons among all possible physics and combinatorial background is

$$\Delta m = m(K^\mp\pi^\pm\pi^\pm_{slow}) - m(K^\mp\pi^\pm). \tag{8.1}$$

8.1 Determination of number of D^* mesons

The separation of D^* mesons contribution from the background can be provided by different methods applied to the Δm distribution. First and the most elementary method is to restrict a range in Δm to the values close to the expected peak position. Naturally this method suffers from a large background. The more elaborate method is a so-called wrong charge subtraction. In this method the Δm distribution of D^* candidates reconstructed from incorrect charge combinations with respect to (8.1) (wrong charge WCH) is normalized to Δm of right charge (RCH defined in (8.1)) candidates in a control region where no D^* signal is expected. Then the wrong charge distribution is subtracted from the right charge one. This method is often used but is not so suitable for small statistic where large fluctuations appear. The third method which was in the end used for this analysis is fit of Δm distribution by the composite function.

8.2 Maximum likelihood fitting method

Due to the small statistics of VFPS data, the decision to use the unbinned likelihood fits was made. The likelihood function $\mathcal{L}$ for independent set of data can be expressed as

$$\mathcal{L} = \prod_{i=1}^{N} P(x_i|\alpha), \tag{8.2}$$

where $P(x_i|\alpha)$ is the probability density function depending on parameter α evaluated for data value x_i in a given set of N measurements. The parameter α that maximizes the likelihood function is called maximum likelihood estimator [36]. The simple example can be shown for the Gaussian signal. The probability density function for x_i equals to

$$P(x_i|\mu,\sigma) = \frac{1}{\sqrt{2\pi}\sigma} e^{-\frac{(x_i-\mu)^2}{2\sigma^2}}. \tag{8.3}$$

An easier way to operate with likelihood is to logarithm the likelihood function and thus convert the multiplication to addition for a given data set. After logarithm operation the equation (8.3) is given by

$$\ln \mathcal{L} = constant - \sum_{i=1}^{N} \frac{(x_i - \mu)^2}{2\sigma^2}, \tag{8.4}$$

where constant is independent of μ. To obtain the best value of μ the maximum of likelihood must be found. The standard deviation of μ value can be estimated as

$$\sigma = \sqrt{\frac{-1}{\frac{\mathrm{d}^2 \ln \mathcal{L}}{\mathrm{d}\mu^2}}}. \tag{8.5}$$

Among the advantages of maximum likelihood method belong the easiness to use and no need of binning. Unbinned maximum likelihood method is usually the most powerful method for fitting with satisfying performance even for small statistics.

The unbinned maximum likelihood method is implemented into ROOT by RooFit library using MINUIT for minimization process [37]. In this program, the extended likelihood fits are also possible. The extended likelihood differs from the standard one by the fact that the normalizations of the probability functions can be varied. And thus is applicable for measurements, where the numbers of signal and background events have to be estimated [38].

8.3 Using the maximum likelihood for Δm fits

In this study number of D^* mesons was obtained from the total Δm distribution using extended unbinned maximum likelihood fit described in subsection 8.2. Due to the presence of the background the fitted function comprises signal and background component. In order to determine the background more precisely, the simultaneous fit of right and wrong charge distributions was performed, where the later one was fitted with the probability distribution of background only. In this analysis, the background is the best parametrized by the power function. For fitting the D^* signal often applied function is Crystal Ball due to the asymmetric character of Δm peak. The Crystal Ball function named after Crystal Ball Collaboration is defined for measured quantity W as follows

$$f(W) = N. \begin{cases} e^{-\frac{(W-W')^2}{2\sigma^2}}, & \frac{W-W'}{\sigma} \geq -\alpha \\ (\frac{x}{|\alpha|})^x e^{\frac{-\alpha^2}{2}} [\frac{\sigma}{W'-W+\sigma(x/|\alpha|-|\alpha|)}]^x, & \frac{W-W'}{\sigma} < -\alpha, \end{cases} \tag{8.6}$$

where N is the normalization factor and α, W', σ, x are parameters [39].

But due to the small statistics the Crystal Ball function could not be used in this analysis and Gaussian function was used instead. The final fitting function for the right charge distribution is

$$f_{RCH}(\Delta m) = N_{sig} \frac{1}{\sqrt{2\pi\sigma^2}} e^{-\frac{(\Delta m - m_0)^2}{2\sigma^2}} + N_{bkg}^{(RCH)} (\Delta m)^p, \tag{8.7}$$

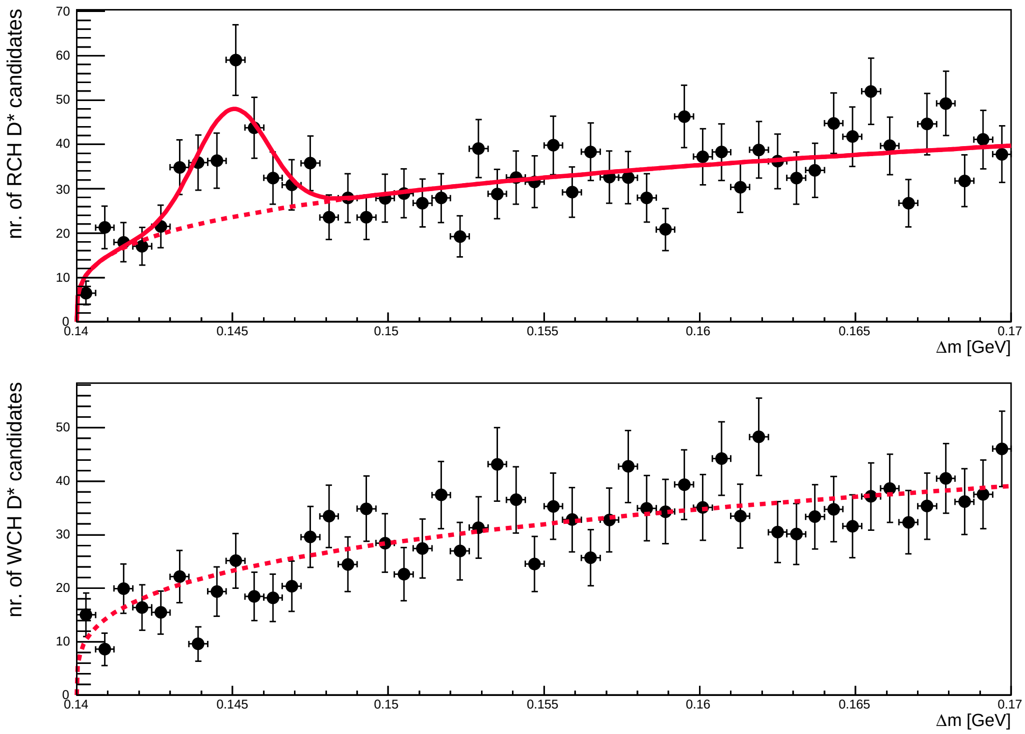

Figure 8.1: Simultaneous fit of right (top) and wrong (bottom) charge distribution of Δm in data.

where N_{sig} is the number of signal events, parameter $N_{bkg}^{(RCH)}$ is related with the number of background events, σ, m_0 and p are the additional parameters.

For the wrong charge distribution fit the function

$$f_{WCH}(\Delta m) = N_{bkg}^{(WCH)}(\Delta m)^p \tag{8.8}$$

is used. The $N_{WCH}^{(BKG)}$ determines the wrong charge distribution normalization. Parameter p is shared for both distributions, thus simultaneous fit is performed.

The number of D^* mesons in data was determined by this method to be

$$N(D^*)_{DATA} = 119 \pm 23, \tag{8.9}$$

the simulation predicts the number of D^* mesons to be

$$N(D^*)_{MC} = 100 \pm 4. \tag{8.10}$$

The fitted Δm distributions of data and simulation are shown in Fig. 8.1 and 8.2. Note in Fig. 8.2 the obvious difference in the signal to background ratio with respect to the data fit in Fig. 8.1. This is caused by the fact that only the charm MC is used for this analysis (signal is enhanced). Also the different shape of the signal peak in Δm can be seen. There is no easy solution of this problem and it has been observed many times in H1 [26], causing no harm to this kind of analysis. The value of $N(D^*)_{MC}$ is based on raw MC statistics 1717 events, the value 100 was obtained by the normalization to the luminosity of data.

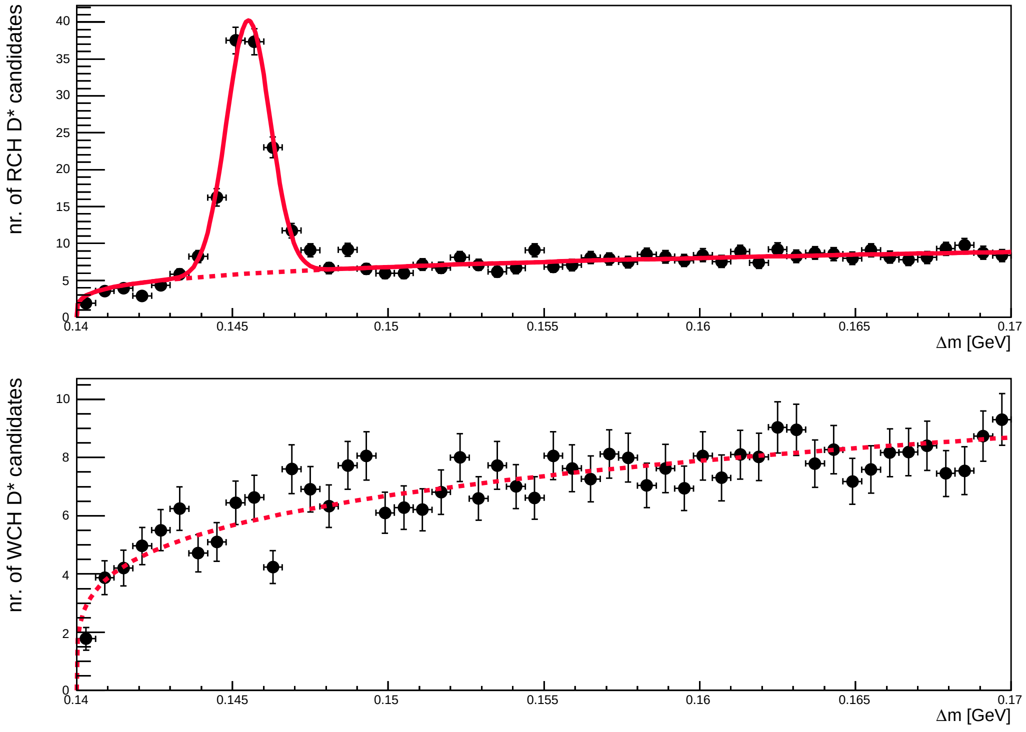

Figure 8.2: Simultaneous fit of right (top) and wrong (bottom) charge distribution of Δm in the simulation.

9. Control plots

Control distributions provide information about the description of data by MC detector simulation. Good agreement of data and simulation is expected but, in general, there are reasons for disagreement. First, the model implemented in MC generator RAPGAP may not correspond to the physics reality. This discrepancy can be then easily eliminated by a reweighting procedure. The second reason is that the efficiency can be wrong in given region. The reasonable agreement of data and simulation is also required for a bin-by-bin correction method introduced in Sec. 10.1.

9.1 Control plots from fits

Control distributions are plots where D^* signal is shown in bins of kinematic variables. This signal is obtained from fits described in section 8.3. Choice of binning for these plots was based on the requirement of reasonable statistics in each bin because fits with low number of signal events often tend to fail to converge. Because a correct normalization of MC is not expected, in following control plots the distributions of simulations are normalized to the number of D^* mesons in data.

In the Fig. 9.1 control plots in x_{IP}, $\eta(D^*)$, $p_t(D^*)$ and y_h are shown. Fig. 9.2 shows the control distribution of the primary vertex z-coordinate position z_{vtx}.

As it can be seen the control plots suffer from large fluctuations due to small data statistics. The attempt to reweight the MC control distributions on hadron level could be made, but it is questionable whether this is needed whatsoever given the large statistical uncertainties of the data. The ambiguity of reweighting would definitely considerably contribute to a systematic uncertainty of the cross section measurement (Sec. 10.1). Evaluation of the systematic uncertainties is however beyond the scope of the thesis. In spite of these fluctuations, the data and simulations agree within the statistical uncertainties.

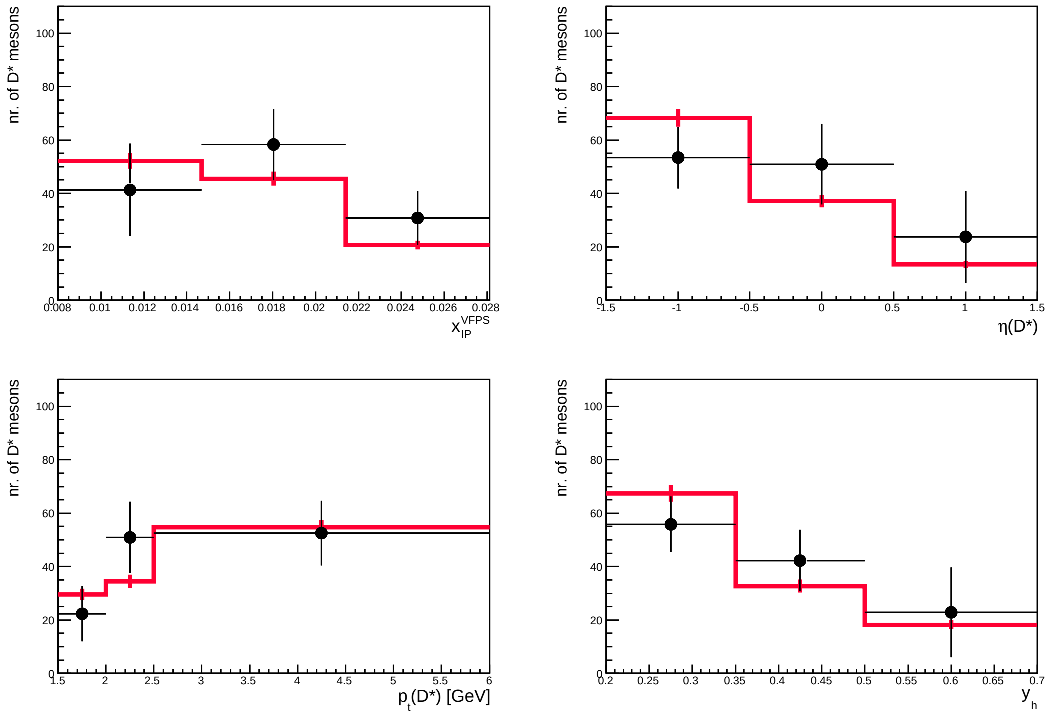

Figure 9.1: Control distributions in x_{IP}^{VFPS}, $\eta(D^*)$, $p_t(D^*)$, y_h. Dots are data, lines correspond to the MC simulations. The data points and MC predictions are shown with the statistical uncertainties.

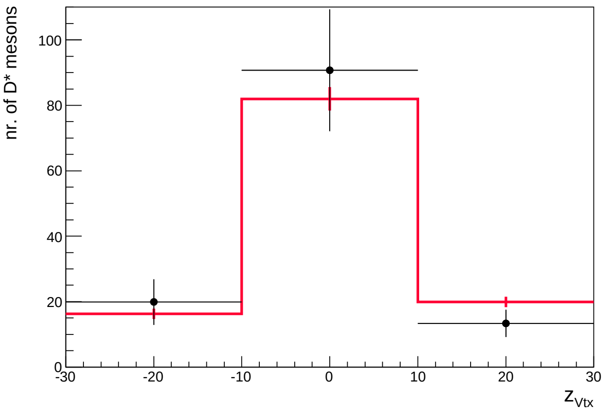

Figure 9.2: Control distribution in z_{vtx}. Dots are data, lines correspond to the MC simulations. The data points and MC predictions are shown with the statistical uncertainties.

10. Cross section determination

To make any conclusions about the nature of processes in physics the data not affected by detection are required. Because the detectors suffer from the limited acceptance, resolution and efficiency, the methods which correct the data to the detector effects have to be introduced. There are basically two methods how the measured quantities can be corrected to such effects, matrix unfolding and bin-by-bin correction method [40]. Here only the bin-by-bin correction method will be described. This method is often utilized in high-energy physics experiments because it is easier to use than the matrix unfolding.

The essential assumption which validates the use of bin-by-bin correction method is a satisfactory description of data by simulation. A reasonable agreement of data and simulation was already shown in Sec. 9.1. Because data are usually corrected to the level of stable hadrons one needs to use the MC simulations which provide the reconstructed and hadron (true) level information at the same time.

10.1 Cross section formula, bin-by-bin method

The classical formula for the total diffractive D^* photoproduction cross section is given by

$$\sigma(ep \to eD^*X'p) = \frac{N(D^*)_{DATA}}{\mathcal{L}\, BR(D^* \to K\pi\pi_{slow})\, A}, \tag{10.1}$$

where $N(D^*)_{DATA}$ denotes number of D^* mesons obtained from the extended unbinned maximum likelihood fits (see Fig. 8.1) in data. X' is the rest of the hadronic final state, $\mathcal{L}$ is the total integrated luminosity of data, BR branching ratio of the golden decay channel [18], A the detector acceptance, which includes the efficiency of trigger simulated in MC.

A more elaborate definition often used in H1 analyses is [41]

$$\sigma(ep \to eD^*X'p) = \frac{N(D^*)_{DATA} - N(D^*)_{MC,\,BKG}}{\mathcal{L}\, BR(D^* \to K\pi\pi_{slow})\, A_D}, \tag{10.2}$$

where $N(D^*)_{MC,\,BKG}$ is number of reconstructed D^* candidates which migrate into the measured phase space from outside the hadron level phase space domain (see Tab. 7.5). Further A_D is a modified detector acceptance defined in Sec. 10.1.1.

In the presented analysis the amount of background events $N(D^*)_{MC,\,BKG}$ is small and it was difficult to perform a stable fit, so the definition (10.1) was used.

10.1.1 Acceptance, stability and purity

The bin-by-bin correction method is based on the use of acceptance correction factors. If cross section is supposed to be measured differentially (in bins of certain observable) the following numbers need to be determined from the MC Rapgap:

- N_i^{gen} – denotes the number of D^* mesons in bin i on the hadron level which passed the hadron level kinematic cuts in Tab. 7.5
- N_i^{rec} – denotes the number of D^* mesons in bin i on the detector level which passed the kinematic cuts on detector level described in section 7.3, tables 7.1, 7.2, 7.3, 7.4
- $N_i^{gen\&\&rec}$ – denotes the number of D^* mesons reconstructed in bin i which passed the kinematic cuts on both levels
- $N_i^{gen_j\&\&rec_i}$ – denotes the number of D^* mesons reconstructed in bin i and generated in bin j which passed the kinematic cuts on both levels

Then the acceptance is given by

$$A_i = \frac{N_i^{rec}}{N_i^{gen}}, \tag{10.3}$$

expressing the ratio of events which were observed on the detector level to the number of generated events.

For the formula (10.2) the acceptance is defined as follows

$$A_{D\,i} = \frac{N_i^{gen\&\&rec}}{N_i^{gen}}, \tag{10.4}$$

The total acceptance in this definition is equal to the total stability (defined bellow).

Further the quantities purity P and stability S can be introduced in order to tell us more about the detector effects. The purity is defined as

$$P_i = \frac{N_i^{gen_i\&\&rec_i}}{N_i^{rec}}, \tag{10.5}$$

i.e. the number of D^* mesons generated and reconstructed in the same bin to the number of all reconstructed D^* mesons in bin i. Evidently, the purity gives information about each bin in the sense of the ratio of the reconstructed D^* mesons which originate from the same hadron level bin to all reconstructed D^* mesons in bin i, thus the migrations among bins and also migrations from outside the hadron level phase space are evaluated.

Analogous quantity meaning the fraction of D^* mesons which were generated as well as reconstructed in one bin to all generated events in the bin i is called stability and defined by formula

$$S_i = \frac{N_i^{gen_i\&\&rec_i}}{N_i^{gen}}. \tag{10.6}$$

Obviously these three quantities are tied up with equation

$$A_i = \frac{S_i}{P_i}. \tag{10.7}$$

The bin-by-bin correction method is applicable for cases where low migration effects occur. Such information is provided by purity which states the percentage of events which do belong to the measured bin. Purity is generally required to be above 75%. In order to use the bin-by-bin correction method, the binning of differential cross sections cannot be chosen arbitrarily, but bin purities have to be evaluated.

10.1.2 Bin-by-bin correction results

The bin acceptances, purities and stabilities in kinematic variables $p_t(D^*)$, $\eta(D^*)$, x_{IP}^{VFPS} and y_h, in which the differential cross sections will be shown, are depicted in Fig. 10.1. Total acceptance, purity and stability are shown in Fig. 10.2. The acceptance definition 10.3 was chosen.

Analyzing the Fig. 10.1 several conclusions can be made. Purities for $\eta(D^*)$ and $p_t(D^*)$ are very high – around 80% and higher, so rather small migrations between bins are present. This is result of a good reconstruction shown in correlation plots 6.2 and 6.3. The purities for x_{IP}^{VFPS} and y_h are smaller – around 50% and higher, due to the poor correlations between the hadron and detector level (see Fig. 6.4 and Fig. 6.6) and thus larger bin migrations can be seen. The final binning was chosen as a balance between the sufficient bin statistics for fits, satisfactory purities and signal shape visibility in desired variables.

The total purity depicted in Fig. 10.2 provides information about out of the phase space migrations. Percentage of out of the hadron phase space events is given by $1 - P \simeq 13\%$. From mentioned figure, it is obvious that small amount of these events is present, resulting in small $N_{BKG,MC}$ in definition (10.2). Also because the total acceptance is very similar to the total stability, both definitions of total acceptance (10.3), (10.4) give nearly equal results. In consequence, the use of the cross section definition (10.1) is justified. In general the acceptance is small ($\approx 13\%$) what is caused by the VFPS acceptance and D^* selection criteria. Just for the comparison the typical acceptance is around $30\% - 40\%$ [23] for LRG analyses at H1.

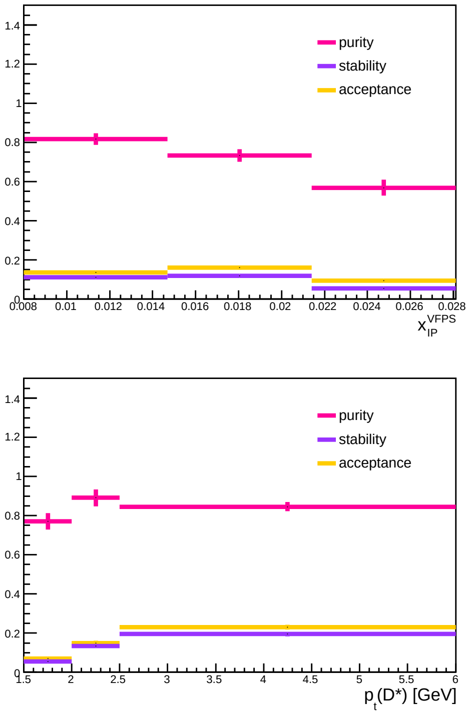

Figure 10.1: Purities P_i (pink), stabilities S_i (violet) and acceptances A_i (yellow) in bins of variables x_{IP}^{VFPS}, $\eta(D^*)$, $p_t(D^*)$ and y_h.

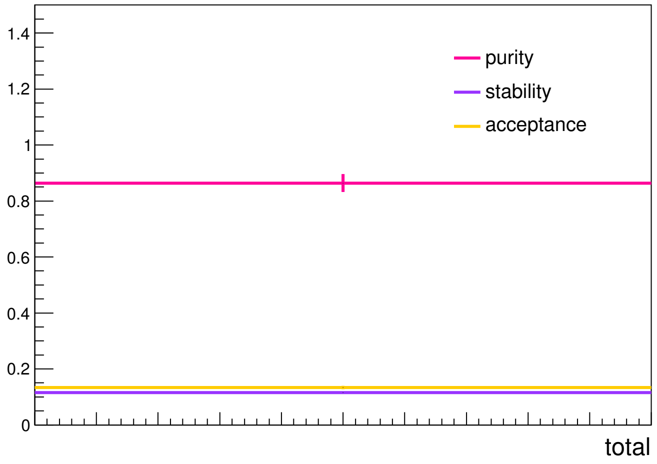

Figure 10.2: Total purity (pink), stability (violet) and acceptance (yellow) in analysed phase space.

11. Results

11.1 Cross section measurement

In this analysis D^* mesons originating from the e^+p diffractive photoproduction and decaying through the golden channel $D^{*\pm} \to K^{\mp}\pi^{\pm}\pi^{\pm}_{slow}$ are investigated. The selection criteria for D^* candidates on the detector level can be found in tables 7.1, 7.2, 7.3, 7.4. The hadron level phase space is described in Tab. 7.5.

Data for the cross section measurement were acquired in years 2006-2007 with the total luminosity $\mathcal{L} = 30.2\,\mathrm{pb}^{-1}$. The number of signal events was obtained by extended unbinned likelihood fit of Δm distribution. As a prediction BGF (c) and resolved γ (c) MC LO generated samples with parton showers were used. These MC samples underwent the detector simulation based on GEANT. The simulated events were processed by the same analysis algorithms as data were.

Presented cross sections of data were corrected for the detector effects using the bin-by-bin correction method. The cross sections of data were compared with the hadron level LO with parton showers MC Rapgap predictions. Because proton dissociation is not present in data but is included in DPDFs, the MC predictions were scaled by 1/1.2 [42]. The formula used for the total cross section calculation is (10.1).

11.2 Total cross section

The total measured cross section of e^+p diffractive photoproduction corrected for the detector effects in kinematic region 7.5 was determined to be

$$\sigma(e^+p \to e^+D^*X'p) = 930 \pm 180\,(\mathrm{stat.})\ \mathrm{pb}. \tag{11.1}$$

In Fig. 11.1 measured cross section is compared with MC Rapgap LO prediction on hadron level. The results are summarized in Tab. 11.1. Within the statistical errors, the MC Rapgap LO cross section prediction is lower than measured cross section. This phenomenon is theoretically understandable because the contribution of NLO is expected to play a considerable role.

The results from previous measurement [20] are summarized in Tab. 11.2. In the previous analysis, for LO predictions, the QCD calculations without parton showers were used. The comparison between presented and previous analysis can be made on the basis of data to MC LO cross section ratio. These ratios are present in tables 11.1, 11.2. It can be concluded, that within statistical errors the ratios of measured cross section to LO prediction are equal. Therefore, the presented measurement is consistent within errors with the previous one in some respect.

As stated in above text the number of measured D^* mesons was expected to be higher than in the previous analysis. The numbers of measured D^* mesons are summarized in Tab. 11.3. Indeed, the statistics in the presented analysis is around 70% higher than in the previous one.

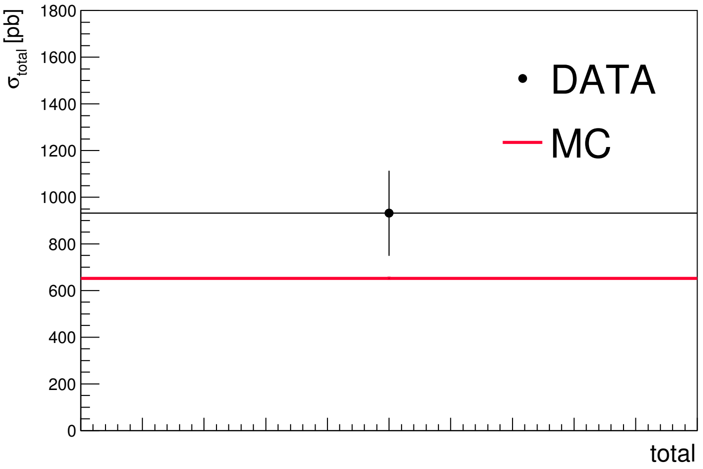

Figure 11.1: Total cross sections. Black dot is the total cross section of data corrected for the detector effects. In pink line the total cross section of MC Rapgap on hadron level is shown. Only statistical uncertainties are present.

Total cross sections of this analysis [pb]	
σ_{DATA}	930 ± 180
$\sigma_{LO,MC}$	653 ± 7
$\frac{\sigma_{DATA}}{\sigma_{LO,MC}}$	1.43 ± 0.28

Table 11.1: Cross section results for data and MC Rapgap and their ratio. All uncertainties are statistical.

Total cross sections of previous H1 analysis [pb]	
σ_{DATA}	265 ± 50 (stat.)
$\sigma_{LO,QCD}$	209
$\sigma_{NLO,Fit\,B}$	$359{\pm}^{93}_{75}$
$\frac{\sigma_{DATA}}{\sigma_{LO,MC}}$	1.27 ± 0.24

Table 11.2: Total cross sections for preceding analysis. Cross section results for data, LO and NLO QCD calculations presented in previous analysis [20].

Number of measured D^* mesons	
Presented analysis	119 ± 23
Previous analysis	70 ± 13

Table 11.3: Number of D^* mesons found in data by this and previous analysis [20].

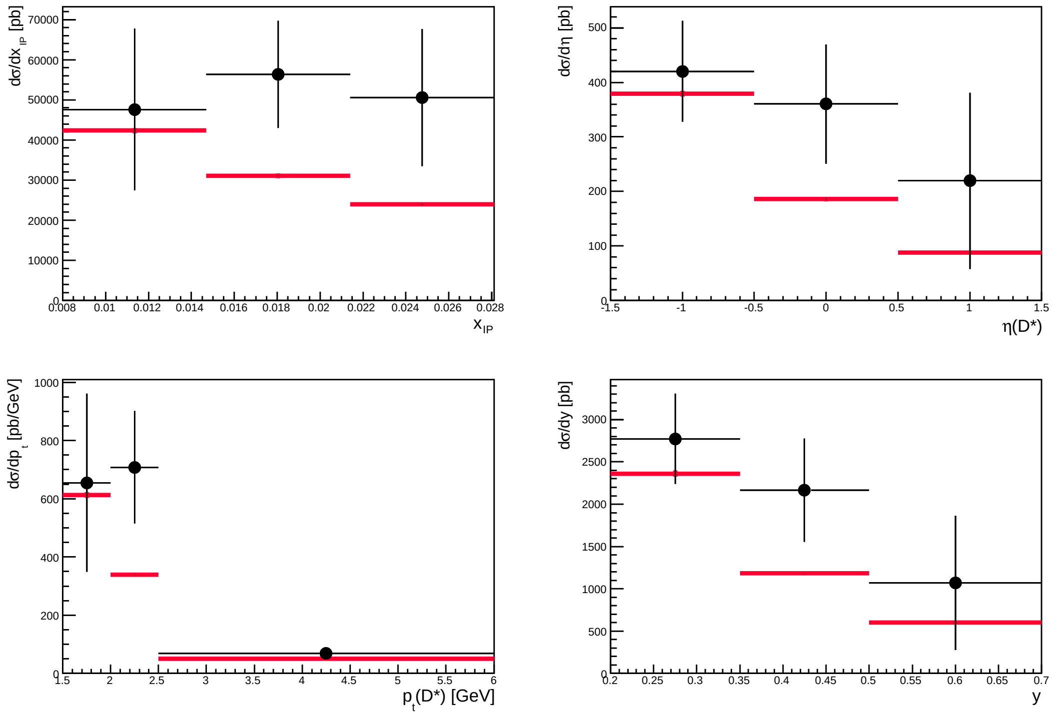

Figure 11.2: Black dots are the differential cross sections of data in x_{IP}, $\eta(D^*)$, $p_t(D^*)$ and y corrected for the detector effects. In pink lines the total cross section of MC Rapgap on hadron level in the same variables are shown. Only statistical uncertainties are presented for both data and MC.

11.3 Differential cross sections

The differential cross sections are shown in two D^* quantities – pseudorapidity $\eta(D^*)$ and transverse momentum $p_t(D^*)$, inelasticity (y) and proton four-momentum loss (x_{IP}). These differential cross sections are depicted in Fig. 11.2. As expected due to low statistics apparent large fluctuations are observed in data shapes with respect to the MC predictions in some variables.

Conclusion

The presented study is the first measurement of the diffractive D^* meson photoproduction where the leading proton was directly detected. The data statistics is higher than in the previous analysis made by H1 collaboration based on the large rapidity gap selection.

The diffractive kinematic region of this study corresponds to the acceptance of Very Forward Proton Spectrometer

$$0.008 < x_{IP} < 0.028,\ |t| < 0.5\,\mathrm{GeV}^2. \tag{11.2}$$

The kinematic region of the photoproduction is defined by the following restrictions on the photon virtuality and inelasticity

$$Q^2 < 2\ \mathrm{GeV}^2,\ 0.2 < y < 0.7. \tag{11.3}$$

The D^* meson kinematics is constrained in transverse momentum and pseudorapidity

$$p_t(D^*) > 1.5\,\mathrm{GeV},\ |\eta(D^*)| < 1.5. \tag{11.4}$$

The total data cross section in phase space described above was measured to be

$$\sigma(e^+p \to e^+D^*X'p) = 930 \pm 180\,(\mathrm{stat.})\ \mathrm{pb}, \tag{11.5}$$

which is 1.4 ± 0.3 times higher than the leading order Monte Carlo Rapgap prediction. This result is within the statistical uncertainty in agreement with the previous analysis where the factor of 1.3 ± 0.2 was seen.

Further the cross section was measured differentially in the fractional proton energy loss x_{IP}, pseudorapidity η and transverse momentum p_t of the D^* meson and the inelasticity y. It can be concluded, that within the statistical uncertainties the Monte Carlo Rapgap predictions describe the shapes of distributions seen in data well.

Part II

Study of LRG selection using VFPS

12. Forward detectors

The diffractive process is characteristic for the gap in rapidities between the scattered proton and the hadronic final state X due to the vacuum quantum numbers exchange. The gap in rapidity (pseudorapidity) $\Delta\eta$ in single dissociative process (Fig. 1.6) is proportional to

$$\Delta\eta \simeq \ln \frac{s}{M^2}, \tag{12.1}$$

where s is the CMS energy of $\gamma^* p$ and M is the mass of hadronic final state X.

Because in diffraction the proton remains unchanged the leading proton tagging method is ideal for studying such processes. But this method suffers from large disadvantage, which is small acceptance of detectors used for proton tagging. Thus, the second approach to the diffraction measurements based on the large rapidity gap condition (LRG) is often used instead. Within this approach no activity above noise levels in forward detectors is required. The statistics using the LRG selection are higher but larger non-diffractive background and proton dissociation components are present. In the following sections, the forward detectors used for the large rapidity gap selection are described.

12.1 Forward Muon Detector (FMD)

The FMD detector consisted of 6 drift chamber planes measuring for polar angles $3^\circ \leq \Theta \leq 17^\circ$, three on either side of a toroidal magnet [43]. Each plane was composed of the double layer of drift cells (r, ϕ measurement). The total number of drift cells was 1520 [43]. The FMD is depicted in Fig. 12.1.

The FMD was forward detector designed for muon identification and measurement. This detector was also capable to measure particles originating from proton remnant and therefore could help with elastic events selection [44]. For diffractive measurements only first three planes in front of the toroidal magnet were used.

The standard cut widely applied in diffractive LRG analyses in H1 reads

$$\texttt{NFmu1} + \texttt{NFmu2} + \texttt{NFmu3} \leq 2 \;\&\&\; \texttt{NFmu1} + \texttt{NFmu2} \leq 1, \tag{12.2}$$

where `NFmu` is number of reconstructed hits in each respective layer. The form of the cut reflects the fact, that the third layer suffered from higher noise levels, therefore one extra hit in `NFmu3` was allowed. The same selection called `FMD cut` is required for this analysis.

12.2 Forward Tagger System (FTS)

FTS was a set of 4 stations at positions 26, 28, 53 and 92 meters from interaction point in the direction of protons. Each station consisted of 4 scintillating counters. These 4 counters were at the same z position placed around the beam pipe. Every counter had two scintillating layers between which the stainless steel was inserted. All stations were sandwiched in the lead in order to protect them from synchrotron radiation [45]. As example FTS at 26 m is shown in Fig. 12.2

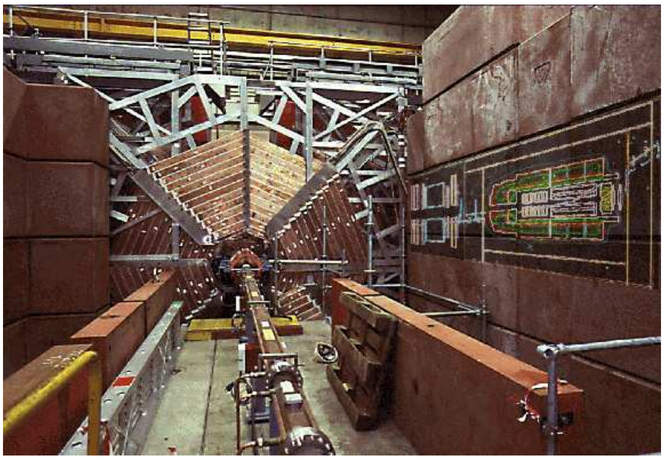

Figure 12.1: Forward Muon Detector (FMD) viewed from the interaction point.

This tagger system was designed for diffractive measurements. Its aim was to select clear diffractive processes without proton dissociative component. FTS measured particles which interacted in beam pipe material or magnets, so FTS was able to detect proton fragments at very large rapidities $6 < \eta < 8$ with good efficiency [46].

Several H1 analyses used only FTS at 26 m with the requirement of no activity for the diffractive events. This criterion was also used as the `FTS cut` in this analysis.

12.3 PLUG calorimeter

The PLUG calorimeter was forward sampling calorimeter designed to fill the gap in acceptance between LAr calorimeter and beam pipe. The detection medium for this detector was silicon and the absorber was made of copper [47]. The region of particles' pseudorapidities measured by PLUG is $3.5 < \eta < 5.1$ [48]. This calorimeter was very useful in tagging of diffractive events because no energy should be deposited in the forward region in diffraction.

The latest H1 diffractive analyses [49] required condition for energy deposited in PLUG $E_{PLUG} < 7\,\mathrm{GeV}$. Therefore in presented study the `PLUG cut` requests the energy deposited in PLUG calorimeter to be less than 7 GeV.

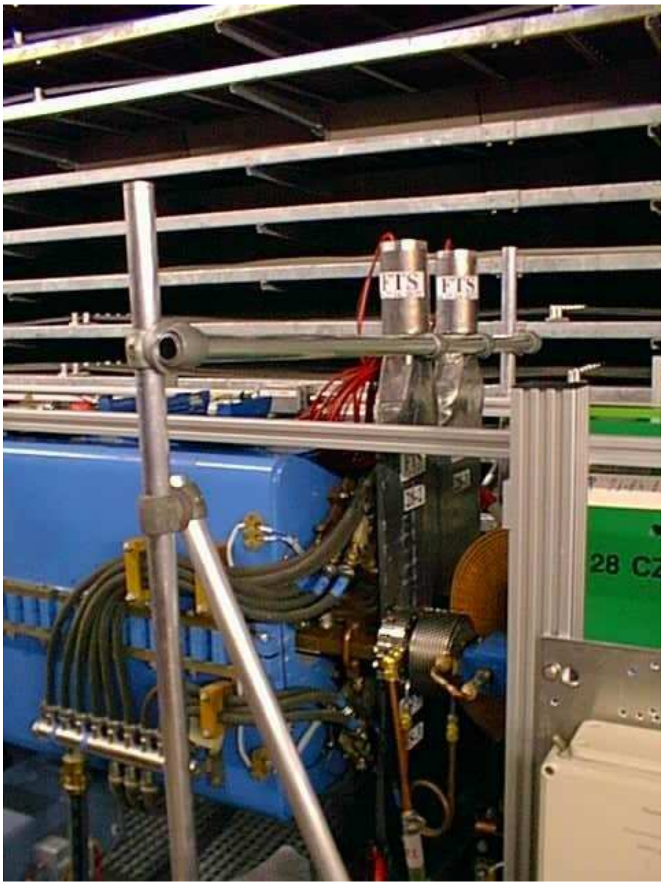

Figure 12.2: Forward Tagger System (FTS) at 26 m.

13. Study of LRG cuts

A standard form of the LRG cuts in H1 can be in general written as

$$\eta_{max} < 3.2 \,\&\&\, \texttt{FMD cut} \,\&\&\, \texttt{FTS cut} \,\&\&\, \texttt{PLUG cut} \tag{13.1}$$

where η_{max} is a pseudorapidity of the most forward cluster in the liquid argon calorimeter with energy above 400 MeV (or 800 MeV). The `FMD`, `FTS` and `PLUG cuts` were defined in Chap. 12.

Since the data sets and MC samples with leading proton are available, there is a unique opportunity to test the response of the forward detectors with genuinely diffractive events. It cannot be expected, that the LRG cuts select the diffractive events with the 100% efficiency, nevertheless the efficiency should be in reasonable agreement with simulation. The simulation is always based on the knowledge of the geometry and material of the detector. Furthermore, realistic noise needs to be taken into an account in the simulation. In conclusion, any difference between the performance of the forward cuts in data and simulation would lead to the systematic uncertainties in the LRG measurements.

13.1 Results of analysis

VFPS data from the same period as in the D^* analysis in part I were used. Also the same VFPS, photoproduction and background cuts were utilized (see Tab. 7.1, 7.2, 7.3). This time, however, the hadronic final state was required to contain two jets with the transverse momenta above 5.5 GeV and 4 GeV for the leading and subleading jet, respectively, found in the laboratory frame with k_T the longitudinally invariant jet algorithm [50]. Further, both jets were required to have pseudorapidities between $-1 < \eta < 2.5$ in the laboratory frame. These selection criteria were needed to be adopted from diffractive dijet photoproduction analysis [24] because the available MC simulations were dedicated specifically to it.

In the following text, the control distributions of observables relevant to the LRG selection will be presented. The distributions of data quantities will be compared with simulated ones. Eventually, fractions of events passing each particular cut in the VFPS sample will be investigated in data and simulation. These fractions are defined as

$$f_{LRG} = \frac{N(LRG \,\&\&\, VFPS)}{N(VFPS)}, \tag{13.2}$$

where $N(LRG \,\&\&\, VFPS)$ denotes the number of events passing the LRG cuts in the VFPS sample and $N(VFPS)$ is the number of events in the VFPS sample. What matters more than the absolute values of f_{LRG} is their data to simulation ratio, because any possible difference between data and MC translates into systematically shifted factors used for the correction of data to the level of stable hadrons (bin-by-bin method in this thesis, unfolding procedure in general).

The fractions f_{LRG} will be analysed as a function of $\log_{10} x_{I\!P}^{VFPS}$. The variable $x_{I\!P}^{VFPS}$ was chosen due to a dependence of the kinematics of system X on the

x_{IP}^{VFPS} value. The higher the x_{IP}^{VFPS} value the more longitudinal energy of the proton is available for the system X.

In Fig. 13.1 the top left and right plots show the distributions of $\eta^{max}(400\,\mathrm{MeV})$ and $\eta^{max}(800\,\mathrm{MeV})$, respectively, for data and MC simulation. It can be seen that the data distributions are not described by simulation. Also from figures it can be deduced that the higher threshold on the most forward cluster energy of 800 MeV indicates a slight improvement of the description, suggesting that the higher noise cut should be preferred in LRG analyses. However, the disagreement between data and simulation cannot be resolved fully. One needs to realize that the η^{max} values also depend on the underlying model implemented in the MC generator which may not be perfect. A common practice in the H1 is to reweight the MC generated spectra in certain variable to obtain a reasonable agreement of MC after simulation with data. This procedure was not applied in this study.

In the figure mentioned above (Fig. 13.1) the bottom left and right plots show the fractions f_{LRG} for data, simulation and their ratio, respectively, as a function of $\log_{10} x_{IP}^{VFPS}$. The effect of non-description of the η^{max} spectra directly translates to the f_{LRG} values, since the η^{max} cut merely integrates number of events above/below the cut value of 3.2. The f_{LRG} decreases for both data and simulation and their ratio deviates from unity at largest x_{IP}^{VFPS} values. If the above mentioned reweighting of the MC generator kinematics were applied one would expect a consistency of the $f_{LRG}^{MC}/f_{LRG}^{data}$ ratio with unity at the level given by the statistical errors.

The Fig. 13.2 shows control distributions of the number of FMD hits in the three pre-toroidal layers, number of FTS hits and energy measured in the PLUG calorimeter. Again the cuts on FTS and PLUG represent a simple cut in the distribution. For FMD, the cuts form makes the visualisation of the cut less obvious. In general, as expected, the diffractive events (ensured by VFPS) contribute mainly at values representing low activity seen by the forward detectors. An attempt to alter the underlying physics model in MC generator (the reweighting mentioned earlier) would be a complicated task for FMD, FTS and PLUG and has not been done by the H1 collaboration. There have been studies that it has been rather the simulation (geometry, efficiency, calibration) that might have needed corrections. Here, unlike the η^{max} case, the LRG fractions without referring to any possible improvements are studied.

The fractions f_{LRG} for FMD, FTS and PLUG are shown in Fig. 13.3 also as function $\log_{10} x_{IP}^{VFPS}$ for both data and simulation as well as their ratio. As it can be seen the FMD data to simulation fraction ratio (the one that matters the most) fluctuates significantly and a variation of about 10% around unity would cover the ratio with its deviations. In the plots for FTS and PLUG (Fig. 13.3) the data to simulation ratios are consistent with unity at about 4% level.

The results obtained on the absolute values of f_{LRG} in data a and simulation and their ratio must be understood in the way that they validate the choice of LRG cuts for the diffractive events (in a specific range of kinematics) and they provide some idea on impact of possible difference between the performance of the forward detectors in data and the implementation in simulation.

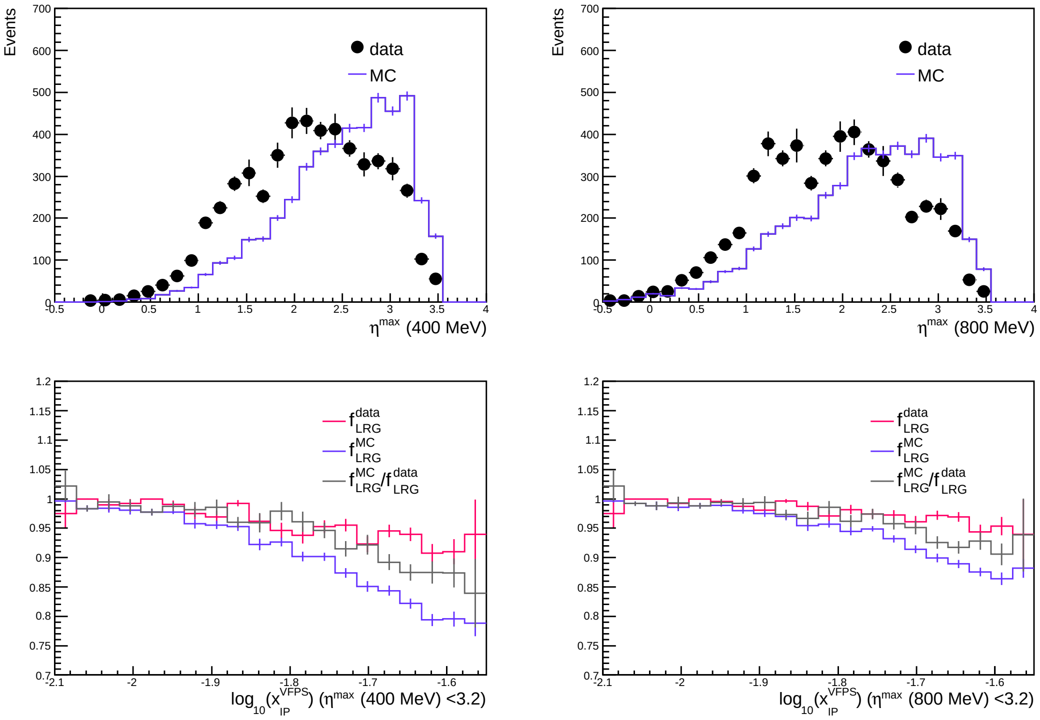

Figure 13.1: Top left and right plots show distributions in data and simulation of pseudorapidity of the most forward cluster η^{max} with the energy threshold 400 MeV and 800 MeV, respectively. The bottom two shows the fractions in data, simulation and their ratios in $\log_{10}(x_{IP}^{VFPS})$, applying cut $\eta^{max} < 3.2$ for energy threshold 400 MeV and 800 MeV, respectively.

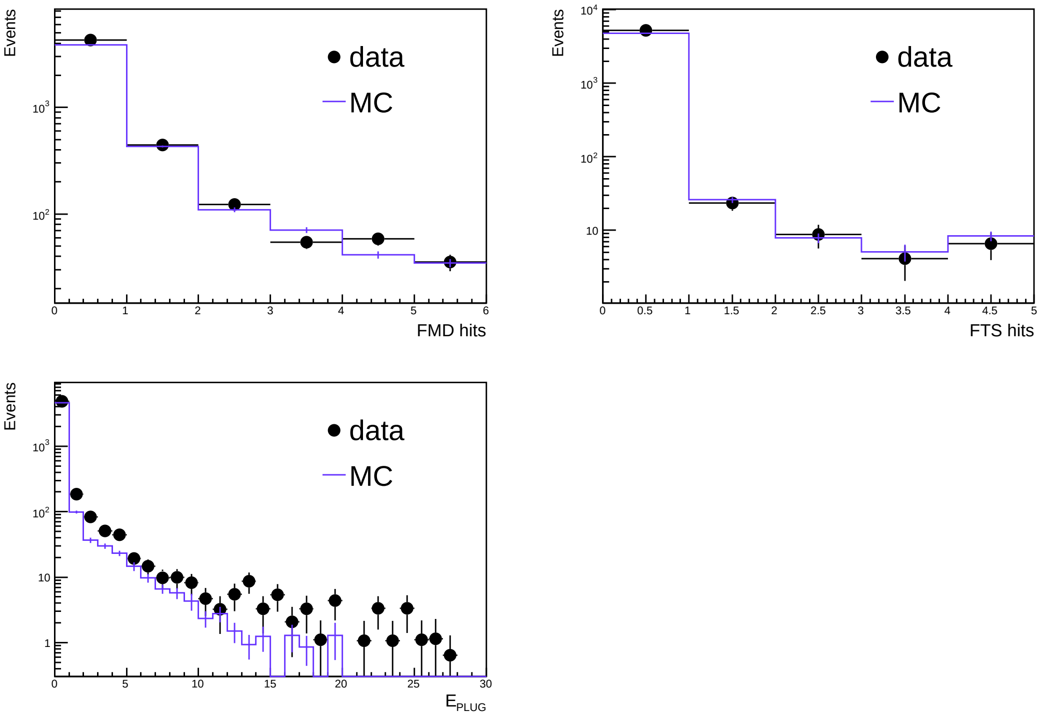

Figure 13.2: Control distributions in FMD and FTS hits and energy deposited in the PLUG calorimeter E_{PLUG}. Data are shown in dots while simulations in the violet lines.

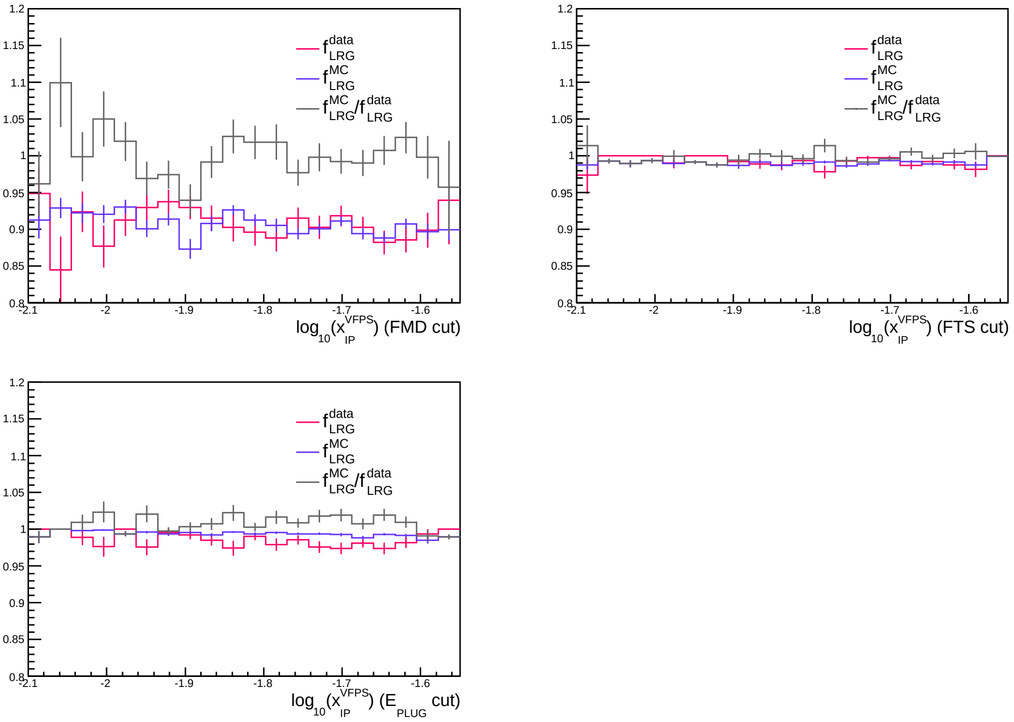

Figure 13.3: The fractions in data, simulation and their ratios in $\log_{10}(x_{IP}^{VFPS})$, applying FMD, FTS and PLUG cuts, respectively.

Bibliography

[1] C. Quigg, *Gauge Theories of the Strong, Weak and Electromagnetic Interactions*. Princeton University Press, New Jersey, second ed., 2013.

[2] D. Griffiths, *Introduction to Elementary Particles*. WILEY-VCH Verlag GmbH & Co. KGaA, Weinheim, second ed., 2008.

[3] J. Chýla, "Quarks, partons and Quantum Chromodynamics." `http://www-hep2.fzu.cz/Theory/notes/text.pdf`, 2003.

[4] E. D. Bloom, D. H. Coward, H. DeStaebler, J. Drees, G. Miller, L. W. Mo, R. E. Taylor, M. Breidenbach, J. I. Friedman, G. C. Hartmann, and H. W. Kendall, "High-Energy Inelastic $e - p$ Scattering at 6° and 10°," *Phys. Rev. Lett.* **23** (Oct, 1969) 930–934. `http://link.aps.org/doi/10.1103/PhysRevLett.23.930`.

[5] J. Žáček, *Úvod do fyziky elementárních částic*. Karolinum, Prague, first ed., 2005.

[6] H. Fritzsch, M. Gell-Mann, and H. Leutwyler, "Advantages of the Color Octet Gluon Picture," *Phys.Lett.* **B47** (1973) 365–368.

[7] **H1** Collaboration, F. Aaron *et al.*, "Inclusive Deep Inelastic Scattering at High Q^2 with Longitudinally Polarised Lepton Beams at HERA," *JHEP* **1209** (2012) 061, `arXiv:1206.7007 [hep-ex]`.

[8] G. Chew and S. C. Frautschi, "Regge Trajectories and the Principle of Maximum Strength for Strong Interactions," *Phys.Rev.Lett.* **8** (1962) 41–44.

[9] A. Donnachie and P. Landshoff, "Total cross-sections," *Phys.Lett.* **B296** (1992) 227–232, `arXiv:hep-ph/9209205 [hep-ph]`.

[10] L. L. Foldy and R. F. Peierls, "Isotopic Spin of Exchanged Systems," *Phys.Rev.* **130** (1963) 1585–1589.

[11] A. Abrikosov, A. Galanin, L. Gorkov, L. Landau, I. Y. Pomeranchuk, *et al.*, "Possibility of Formulation of a Theory of Strongly Interacting Fermions," *Phys.Rev.* **111** (1958) 321–328.

[12] V. Barone and E. Predazzi, *High-Energy Particle Diffraction*. Springer, Heidelberg, first ed., 2002.

[13] G. Ingelman and P. Schlein, "Jet Structure in High Mass Diffractive Scattering," *Phys.Lett.* **B152** (1985) 256.

[14] **UA8** Collaboration, R. Bonino *et al.*, "Evidence for Transverse Jets in High Mass Diffraction," *Phys.Lett.* **B211** (1988) 239.

[15] **H1** Collaboration, T. Ahmed *et al.*, "Deep inelastic scattering events with a large rapidity gap at HERA," *Nucl.Phys.* **B429** (1994) 477–502.

[16] J. C. Collins, "Proof of factorization for diffractive hard scattering," *Phys.Rev.* **D57** (1998) 3051–3056, `arXiv:hep-ph/9709499 [hep-ph]`.

[17] **H1** Collaboration, A. Aktas *et al.*, "Measurement and QCD analysis of the diffractive deep-inelastic scattering cross-section at HERA," *Eur.Phys.J.* **C48** (2006) 715–748, `arXiv:hep-ex/0606004 [hep-ex]`.

[18] **Particle Data Group** Collaboration, K. Olive *et al.*, "Review of Particle Physics," *Chin.Phys.* **C38** (2014) 090001.

[19] A. Astvatsatourov, K. Cerny, J. Delvax, L. Favart, T. Hreus, *et al.*, "The H1 very forward proton spectrometer at HERA," *Nucl.Instrum.Meth.* **A736** (2014) 46–65.

[20] **H1** Collaboration, A. Aktas *et al.*, "Diffractive open charm production in deep-inelastic scattering and photoproduction at HERA," *Eur.Phys.J.* **C50** (2007) 1–20, `arXiv:hep-ex/0610076 [hep-ex]`.

[21] **CDF** Collaboration, T. Affolder *et al.*, "Diffractive dijets with a leading antiproton in $\bar{p}p$ collisions at $\sqrt{s} = 1800$ GeV," *Phys.Rev.Lett.* **84** (2000) 5043–5048.

[22] **H1** Collaboration, A. Aktas *et al.*, "Tests of QCD factorisation in the diffractive production of dijets in deep-inelastic scattering and photoproduction at HERA," *Eur.Phys.J.* **C51** (2007) 549–568, `arXiv:hep-ex/0703022 [hep-ex]`.

[23] **H1** Collaboration, F. Aaron *et al.*, "Diffractive Dijet Photoproduction in ep Collisions at HERA," *Eur.Phys.J.* **C70** (2010) 15–37, `arXiv:1006.0946 [hep-ex]`.

[24] **H1** Collaboration, V. Andreev *et al.*, "Diffractive Dijet Production with a Leading Proton in ep Collisions at HERA," `arXiv:1502.01683 [hep-ex]`.

[25] **ZEUS** Collaboration, S. Chekanov *et al.*, "Diffractive photoproduction of dijets in ep collisions at HERA," *Eur.Phys.J.* **C55** (2008) 177–191, `arXiv:0710.1498 [hep-ex]`.

[26] R. Wolf, *Messung diffraktiver $D^{*\pm}$-Meson Produktion in tief-inelastischer ep-Streuung un Photoproduktion bei HERA*. PhD thesis, Naturwissenschaftlich-Mathematischen Gesamtfakultat der Ruprecht-Karls-Universitat Heidelberg, 2006.

[27] **H1** Collaboration, "The H1 detector at HERA." `http://www-h1.desy.de/h1det/`, Last modified Oct 11, 2002 [cited: Apr 28, 2015].

[28] H. Bethe and W. Heitler, "On the Stopping of fast particles and on the creation of positive electrons," *Proc.Roy.Soc.Lond.* **A146** (1934) 83–112.

[29] **H1** Collaboration, I. Abt *et al.*, "The Tracking, calorimeter and muon detectors of the H1 experiment at HERA," *Nucl.Instrum.Meth.* **A386** (1997) 348–396.

[30] **H1** Collaboration, L. Favart, "Proposal for a very forward proton spectrometer in H1 after 2000," `arXiv:hep-ph/0006167 [hep-ph]`.

[31] M. H. Seymour and M. Marx, "Monte Carlo Event Generators," `arXiv:1304.6677 [hep-ph]`.

[32] H. Jung, "The RAPGAP Monte Carlo for Deep Inelastic Scattering," 2006.

[33] M. Gluck, E. Reya, and A. Vogt, "Parton structure of the photon beyond the leading order," *Phys.Rev.* **D45** (1992) 3986–3994.

[34] B. Andersson, G. Gustafson, G. Ingelman, and T. Sjostrand, "Parton Fragmentation and String Dynamics," *Phys.Rept.* **97** (1983) 31–145.

[35] R. Brun, F. Carminati, and S. Giani, "GEANT Detector Description and Simulation Tool,".

[36] G. Cowan, *Statistical Data Analysis.* CLARENDON PRESS, Oxford, 1998.

[37] W. Verkerke and D. Kirkby, *RooFit Users Manual v2.91*, 2008.

[38] R. J. Barlow, "Extended maximum likelihood," *Nucl.Instrum.Meth.* **A297** (1990) 496–506.

[39] J. Gaiser, "Charmonium Spectroscopy From Radiative Decays of the J/ψ and ψ',".

[40] V. Blobel, "Unfolding Methods in High-energy Physics Experiments,".

[41] S. Schmitt, "Correction of detector effects: bin-by-bin and unfolding," *H1 internal note* (2011) 1–10.
Available at `http://www-h1.desy.de/general/home/intra_home.html`.

[42] F. Aaron, C. Alexa, V. Andreev, S. Backovic, A. Baghdasaryan, *et al.*, "Measurement of the cross section for diffractive deep-inelastic scattering with a leading proton at HERA," *Eur.Phys.J.* **C71** (2011) 1578, `arXiv:1010.1476 [hep-ex]`.

[43] P. Biddulph, H. Cronstrom, P. Finnegan, J. Foster, S. Gilbert, *et al.*, "The H1 forward muon spectrometer," *Nucl.Instrum.Meth.* **A340** (1994) 304–308.

[44] A. Mehta, "Measurement of the diffractive proton structure function and calibration of the forward muon detector at H1,".

[45] V. Solochenko, "Forward Tagging System." `http://hera1.in2p3.fr/throng_dir/h1/h1sim/h1sim33101/manual/chaps.html`, Last modified Jan 31, 1998 [cited: Apr 28, 2015].

[46] **H1** Collaboration, "The Forward Tagger System of the H1 Experiment." `https://www-h1.desy.de/h1/iww/idet/itracker/ifts/index.html`, [cited: Apr 28, 2015].

[47] W. Hildesheim and M. Seidel, "An Investigation into the radiation damage of the silicon detectors of the H1 PLUG calorimeter within the HERA environment," `arXiv:hep-ex/9507013 [hep-ex]`.

[48] E. Panaro, "Energy measurements in e p collisions at HERA using the PLUG calorimeter of the H1 experiment,".

[49] **H1** Collaboration, F. Aaron *et al.*, "Inclusive Measurement of Diffractive Deep-Inelastic Scattering at HERA," *Eur.Phys.J.* **C72** (2012) 2074, `arXiv:1203.4495 [hep-ex]`.

[50] S. Catani, Y. L. Dokshitzer, and B. Webber, "The K^- perpendicular clustering algorithm for jets in deep inelastic scattering and hadron collisions," *Phys.Lett.* **B285** (1992) 291–299.